



# LUND UNIVERSITY

## Optical investigations and characterization of soot of different morphology and maturity

Török, Sandra

2021

*Document Version:*

Publisher's PDF, also known as Version of record

[Link to publication](#)

*Citation for published version (APA):*

Török, S. (2021). *Optical investigations and characterization of soot of different morphology and maturity*. Department of Physics, Lund University.

*Total number of authors:*

1

### General rights

Unless other specific re-use rights are stated the following general rights apply:

Copyright and moral rights for the publications made accessible in the public portal are retained by the authors and/or other copyright owners and it is a condition of accessing publications that users recognise and abide by the legal requirements associated with these rights.

- Users may download and print one copy of any publication from the public portal for the purpose of private study or research.
- You may not further distribute the material or use it for any profit-making activity or commercial gain
- You may freely distribute the URL identifying the publication in the public portal

Read more about Creative commons licenses: <https://creativecommons.org/licenses/>

### Take down policy

If you believe that this document breaches copyright please contact us providing details, and we will remove access to the work immediately and investigate your claim.

LUND UNIVERSITY

PO Box 117  
221 00 Lund  
+46 46-222 00 00

The background of the cover is a grayscale electron micrograph of soot particles. The particles are dark, irregular, and form a complex, branching, fractal-like structure. The structure is composed of many small, spherical primary particles that have aggregated into a larger, interconnected network. The overall appearance is that of a porous, fibrous material.

# Optical investigations and characterization of soot of different morphology and maturity

SANDRA TÖRÖK

DEPARTMENT OF PHYSICS | FACULTY OF ENGINEERING | LUND UNIVERSITY



Optical investigations and characterization  
of soot of different morphology and maturity





# Optical investigations and characterization of soot of different morphology and maturity

Sandra Török



**LUND**  
UNIVERSITY

DOCTORAL DISSERTATION

by due permission of the Faculty of Engineering, Lund University, Sweden.

To be defended at Rydbergsalen, Fysicum, Professorsgatan 1, Lund.

Friday, 17<sup>th</sup> September 2021 at 13:15.

*Faculty opponent*


Dr. Gregory Smallwood

Metrology Research Centre, National Research Council Canada, Ottawa, Canada

<b>Organization</b> LUND UNIVERSITY Combustion Physics Department of Physics P.O. Box 118, SE-211 00 Lund, Sweden		<b>Document name</b> <b>DOCTORAL DISSERTATION</b>
		<b>Date of issue:</b> August 23, 2021
		<b>CODEN:</b> LUTFD2/TFCP-236-SE
Author: <b>Sandra Török</b>		Sponsoring organization
<b>Title and subtitle</b> Optical investigations and characterization of soot of different morphology and maturity		
<p><b>Abstract</b></p> <p>The formation path from small poorly absorbing incipient soot to larger fractal-like strongly absorbing black soot is extensive, and along this path the optical and physicochemical properties of the soot evolve. Soot emitted into the atmosphere may originate from some stage of this process, which will result in a wide spectrum of carbonaceous aerosols in the atmosphere which may interact with the sun and influence the radiative balance of the earth. In this work, differently matured soot from a mini-CAST soot generator was studied in terms of optical properties and the relation to its physicochemical properties. Various optical diagnostic tools, mainly multi-wavelength extinction, elastic light scattering (ELS), and laser-induced incandescence (LII), but also complementary aerosol instrumentation, were used for these purposes. These tools have provided generic information about soot properties, and additionally the applicability of the methods for soot analysis has been evaluated.</p> <p>Soot from the mini-CAST was found to have properties which range from nm-sized soot with optical properties of brown carbon (BrC) to larger soot aggregates of black carbon (BC) type. It was shown that the BrC type of soot had a refractory soot core with properties similar to young soot. Hence, it was shown to not consist of a BC core with a BrC like coating. Also it was shown that upon heating during thermo-optical analysis in an inert atmosphere that the BrC soot transformed and became more absorbing.</p> <p>LII was used to study the optical properties of soot, and it was shown that the optical properties of mature soot agreed well with results from extinction measurements, but for young soot LII results indicated absorption of slightly more mature soot character. Further analysis of the temperature evolution of the soot in the low fluence regime allowed for estimation of the soot absorption efficiency. Results showed large differences in absorption efficiencies for the differently matured soot and values for the mature soot agreed well with values presented in the literature. Double-pulse LII experiments showed how rapid laser heating induced changes in soot of different maturity. It was shown that the absorption properties were enhanced as a result of thermal annealing for all soot with the strongest effect for young soot. Another effect for young soot (using LII at 532 nm excitation) was an increased fluorescence from vaporized fragments that potentially can interfere with the detection of LII signals.</p> <p>A nephelometer was used to study the elastic scattering by soot particles, and it was investigated if scattering theory could be used to solve the inverse problem and obtain information on the morphological properties. The method appeared feasible as tests revealed good results when compared to results based on micrograph image analysis. The method may be useful for estimation of morphological properties of fractal-like soot, as it provides a faster and less elaborate estimation than microscopy analysis.</p> <p>The findings of this work contribute to the understanding of how differently matured soot interact with electromagnetic radiation, especially for the laser-induced incandescence method. Hence information has been gained on how to optimise the diagnostic potential of LII as well as on limitations in the diagnostics of soot of different maturity.</p>		
<b>Key words</b> Laser induced incandescence, extinction, elastic light scattering, mini-CAST, soot, brown carbon, black carbon, maturity, morphology		
Classification system and/or index terms (if any)		
Supplementary bibliographical information		<b>Language</b> English
<b>ISSN</b> and key title: 1102-8718		<b>ISBN</b> 978-91-7895-971-6 (print) 978-91-7895-972-3 (pdf)
Recipient's notes	<b>Number of pages</b> 88	Price
	Security classification	

I, the undersigned, being the copyright owner of the abstract of the above-mentioned dissertation, hereby grant to all reference sources permission to publish and disseminate the abstract of the above-mentioned dissertation.

Signature



Date: 2021-08-09

# Optical investigations and characterization of soot of different morphology and maturity

Sandra Török

DOCTORAL THESIS

2021



**LUND**  
UNIVERSITY

OPTICAL INVESTIGATIONS AND CHARACTERIZATION OF  
SOOT OF DIFFERENT MORPHOLOGY AND MATURITY

Cover by Sandra Török

pp i-70 © 2021 Sandra Török

Paper I © 2018 The authors

Paper II © 2021 The authors

Paper III © 2021 The authors

Paper IV © 2021 The authors (Manuscript unpublished)

Department of Physics  
Faculty of Engineering  
Lund University

Lund Reports on Combustion Physics, LRCP-236 (2021)

ISBN 978-91-7895-971-6 (print)

ISBN 978-91-7895-972-3 (pdf)

ISSN 1102-8718

ISRN LUTFD2/TFCP-236-SE

Printed in Sweden by Media Tryck, Lund University  
Lund 2021



Media-Tryck is a Nordic Swan Ecolabel  
certified provider of printed material.  
Read more about our environmental  
work at [www.mediatryck.lu.se](http://www.mediatryck.lu.se)

**MADE IN SWEDEN** 

# Abstract

The formation path from small poorly absorbing incipient soot to larger fractal-like strongly absorbing black soot is extensive, and along this path the optical and physicochemical properties of the soot evolve. Soot emitted into the atmosphere may originate from some stage of this process, which will result in a wide spectrum of carbonaceous aerosols in the atmosphere which may interact with the sun and influence the radiative balance of the earth.

In this work, differently matured soot from a mini-CAST soot generator was studied in terms of optical properties and the relation to its physicochemical properties. Various optical diagnostic tools, mainly multi-wavelength extinction, elastic light scattering (ELS), and laser-induced incandescence (LII), but also complementary aerosol instrumentation, were used for these purposes. These tools have provided generic information about soot properties, and additionally the applicability of the methods for soot analysis has been evaluated.

Soot from the mini-CAST was found to have properties which range from nm-sized soot with optical properties of brown carbon (BrC) to larger soot aggregates of black carbon (BC) type. It was shown that the BrC type of soot had a refractory soot core with properties similar to young soot. Hence, it was shown to not consist of a BC core with a BrC like coating. Also it was shown that upon heating during thermo-optical analysis in an inert atmosphere that the BrC soot transformed and became more absorbing.

LII was used to study the optical properties of soot, and it was shown that the optical properties of mature soot agreed well with results from extinction measurements, but for young soot LII results indicated absorption of slightly more mature soot character. Further analysis of the temperature evolution of the soot in the low fluence regime allowed for estimation of the soot absorption efficiency. Results showed large differences in absorption efficiencies for the differently matured soot and values for the mature soot agreed well with values presented in the literature.

Double-pulse LII experiments showed how rapid laser heating induced changes in soot of different maturity. It was shown that the absorption properties were enhanced as a result of thermal annealing for all soot with the strongest effect for young soot. Another effect for young soot (using LII at 532 nm excitation) was an



increased fluorescence from vaporized fragments that potentially can interfere with the detection of LII signals.

A nephelometer was used to study the elastic scattering by soot particles, and it was investigated if scattering theory could be used to solve the inverse problem and obtain information on the morphological properties. The method appeared feasible as tests revealed good results when compared to results based on micrograph image analysis. The method may be useful for estimation of morphological properties of fractal-like soot, as it provides a faster and less elaborate estimation than microscopy analysis.

The findings of this work contribute to the understanding of how differently matured soot interact with electromagnetic radiation, especially for the laser-induced incandescence method. Hence information has been gained on how to optimise the diagnostic potential of LII as well as on limitations in the diagnostics of soot of different maturity.

# Populärvetenskaplig sammanfattning

*Arbetet som presenteras i denna avhandling syftar till att öka förståelsen för hur sotpartiklar av olika mognadsgrad interagerar med ljus med motivet att bidra till kunskap relaterat till sotpartiklars påverkan på klimatet. Syftet är även att utforska hur optisk sotdiagnostik fungerar på sot som inte är helt svart.*

Sotpartiklar i atmosfären är effektiva på att absorbera solljus och omvandla det till värme, vilket gör att de beräknas ha näst störst negativ påverkan på klimatet efter koldioxid. Men osäkerheterna är stora och en del kunskapsglapp måste fyllas för att förstå sotets påverkan bättre. Utöver klimatpåverkan så är sot en luftförorening som p.g.a. sin negativa hälsopåverkan bidrar till att miljontals människor dör i förtid enligt Världshälsoorganisationen (WHO).

Sot, som till största delen består av grundämnet kol, bildas vid ofullständig förbränning. Beroende på förhållandena i förbränningsmiljön och hur länge sotet vistats där, så kan det utsläppta sotets egenskaper variera kraftigt p.g.a. att sotet genomgår en mognadsprocess i förbränningsmiljön. De minsta nybildade omogna sotpartiklarna är brunaktiga och delvis transparenta, medan mogna sotpartiklar som vistats längre i förbränningsmiljön kan vara tiotals gånger större och svarta och absorberar mer effektivt än det brunaktiga sotet. Alltså kan egenskaperna hos det utsläppta sotet variera kraftigt beroende på sotets förbränningshistorik.

Sot som släpps ut i atmosfären kommer vidare att åldras genom att reagera med och beläggas med olika molekyler som också släpps ut vid förbränning eller som redan finns i atmosfären, men också genom att förändras kemiskt då det utsätts för solens UV-strålning. Dessa processer kommer att förändra sotets strålningsegenskaper.

För att kunna göra bra uppskattningar kring sotets påverkan på klimatet så är det viktigt att se till det primära sotutsläppet och förstå dess egenskaper först. I studierna som presenteras i denna avhandling så har sot från en sotgenerator studerats på olika sätt, men framför allt med optiska mättekniker. Sotgeneratoren som blåser bort sotpartiklar ur en liten flamma, kan producera sot med väldigt olika egenskaper genom att man förändrar förbränningsprocessen i flammen och därmed blåser ut sot från olika stadier i sotbildningsprocessen. Dessa olika typer av sot kan sägas efterlikna sot från verkliga förbränningsprocesser så som t.ex. dieselförbränning eller biomassaförbränning.

För att kunna uppskatta sotets påverkan på klimatet så måste man förstå hur det interagerar med solljus, d.v.s. elektromagnetisk strålning mellan ungefär 200 och 2000 nm. Laserbaserade mättekniker erbjuder möjligheten att studera interaktionen mellan ljus och sot i aerosolfas, d.v.s. så som det släpps ut i atmosfären. Att mäta t.ex. hur laserljus vid olika våglängder dämpas då det interagerar med sot kan ge information om hur sotets absorptionsegenskaper varierar med våglängd, vilket kan visa hur pass brunt eller svart sotet är och därigenom ge indikationer om mognadsgrad. Genom att kombinera denna typ av absorptionsmätningar med andra aerosolmättekniker, kan mätresultaten ge en mer komplett bild om sotet, t.ex. hur sotets storlek och sammansättning korrelerar med de optiska egenskaperna. I en av de studier som presenteras i denna avhandling så har denna typ av experiment visat att en aerosols oflyktiga sotkärna kan variera i färg, från svagt absorberande/brunt till svart.

Man kan förenklat säga att sotaggregat utgörs av små relativt sfäriska partiklar med storlekar på ca 10-30 nanometer som sitter ihop i en luftigt förgrenad struktur. Detta innebär att om sotaggregat inte är för stora så kan man tillämpa Rayleigh-teori för att relatera sotets spridningsegenskaper till dess form och materialegenskaper. En av studierna i detta arbete har varit att utreda hur en kommersiell nephelometer, som mäter ljusspridning i olika riktningar och vid olika våglängder, kan användas för att ge information om formen på sotet. Det visade sig att man med en nephelometer kan göra en god uppskattning av sotets form (morfologi) och därmed öppnas möjligheten för att bestämma morfologiska parametrar för sot i aerosolfas.

Laserinducerad inkandescens (LII) är en av de vanligaste teknikerna för sotdiagnostik, och den baseras på att man hettar upp sot till ca 3000-4000 grader med en kort laserpuls för att sedan detektera inkandescensen, d.v.s. svartkroppstrålningen, från sotet. Denna teknik kan användas för att studera olika sotrelaterade parametrar, så som koncentration, storlek och absorptionsegenskaper. Vidare har det gjorts en kartlägningsstudie för att öka kunskapen om hur snabb upphettning av omoget sot påverkar och förändrar sotet. Det visar sig att upphettat omoget sot kommer att ”mogna” och ha förändrade egenskaper. Resultaten innebär att man med laserupphettning innan LII-mätningar kan öka detekterbarheten för omoget sot, men också att man kan behöva ta hänsyn till processer som påverkar sotmognaden när experimentella resultat jämförs med modellering och när långa laserpulser används för sotdiagnostik.

# List of publications

The thesis is based on the following papers, which will be referenced by Roman numerals in the text. The papers are attached to the thesis in the listed order.

- I. **Investigation of the absorption Ångström exponent and its relation to physicochemical properties for mini-CAST soot**  
S. Török, V.B. Malmborg, J. Simonsson, A. Eriksson, J. Martinsson, M. Mannazhi, J. Pagels, and P-E. Bengtsson  
*Aerosol Science and Technology*, 52:7,757-767 (2018)
- II. **Numerical scattering simulations for estimating soot aggregate morphology from nephelometer scattering measurements**  
A. Karlsson, S. Török, A. Roth, and P-E. Bengtsson  
*Journal of Aerosol Science*, 159:105828, (2022)
- III. **Laser-induced incandescence ( $2\lambda$  and  $2C$ ) for estimating absorption efficiency of differently matured soot**  
S. Török, Manu Mannazhi, and P-E. Bengtsson  
*Applied Physics B*, 127(7): 96 (2021)
- IV. **Investigating the influence of rapid laser heating of differently matured soot with double-pulse laser-induced incandescence**  
S. Török, M. Mannazhi, S. Bergqvist, K.C. Le, and P-E. Bengtsson  
*Manuscript to be submitted.*

## Related work

Peer-reviewed publications not included in the thesis.

- A. **Wavelength dependence of extinction in sooting flat premixed flames in the visible and near-infrared regimes**  
J. Simonsson, N-E. Olofsson, S. Török, P-E. Bengtsson, and H. Bladh  
*Applied Physics B*, 119:4, 657-667 (2015)
- B. **Particle profiling and classification by a dual-band continuous-wave lidar system**  
G. Zhao, E. Malmqvist, S. Török, P-E. Bengtsson, S. Svanberg, J. Bood, and M. Brydegaard  
*Applied Optics*, 57:35, 10164-10171 (2018)
- C. **Relating aerosol mass spectra to composition and nanostructure of soot particles**  
V.B. Malmborg, A.C. Eriksson, S. Török, Y. Zhang, K. Kling, J. Martinsson, E. C. Fortner, L. Gren, S. Kook, T . B. Onasch, P.-E. Bengtsson, and J. Pagels  
*Carbon*, 142, 535-546 (2019)
- D. **Optical band gap analysis of soot and organic carbon in premixed ethylene flames: Comparison of in-situ and ex-situ absorption measurements**  
C. Russo, B. Apicella, A. Tregrossi, A. Ciajolo, K. C. Le, S. Török, and P.-E. Bengtsson  
*Carbon*, 158, 89-96 (2020)
- E. **Soot maturity studies in methane-air diffusion flames at elevated pressures using laser-induced incandescence**  
M. Mannazhi, S. Török, J. Gao, and P.-E. Bengtsson  
*Proceedings of the combustion institute*, 38, 1217-1224 (2021)



# The author's contributions

## I. **Investigation of the absorption Ångström exponent and its relation to physicochemical properties for mini-CAST soot**

S. Török, V.B. Malmberg, J. Simonsson, A. Eriksson, J. Martinsson, M. Mannazhi, J. Pagels, and P-E. Bengtsson  
*Aerosol Science and Technology*, 52:7,757-767 (2018)

In this work, an investigation of the optical and physicochemical properties of freshly emitted cold soot from a mini-CAST soot generator is presented. Five types of mini-CAST soot were studied using a multi-wavelength extinction setup, aethalometer, SMPS, SP-AMS and thermo-optical analysis, with or without passing a thermodenuder and an oven. Results show that the absorption wavelength dependence, expressed as the absorption Ångström exponent (*AAE*), varied between 1 and 3.5 for soot with a low and high organic carbon content respectively. Despite using an oven to evaporate all volatiles, it was shown that the *AAE* did not decrease to  $\sim 1$  and the organic carbon fraction of the soot did not vanish for all soot types, hence the elevated *AAE* was related to refractory soot of a substantial organic carbon content.

*I and Vilhelm B. Malmberg planned and performed the experiments. I was main responsible for the optical setup and the related data analysis. I was main responsible for the paper which was written together with Vilhelm, with help from the other co-authors.*

## II. **Numerical scattering simulations for estimating soot aggregate morphology from nephelometer scattering measurements**

A. Karlsson, S. Török, A. Roth, and P-E. Bengtsson  
*Journal of Aerosol Science*, 159:105828, (2021)

The potential of using a commercial nephelometer for estimating morphological properties of freshly emitted soot is investigated in this work. By experiments on differently sized and matured soot from a mini-CAST soot generator in combination with numerical simulations using Rayleigh-Debye-Gans theory, the inverse problem was solved and

estimations of radius of gyration and fractal dimension could be estimated in the Guinier and transition regime.

*I was responsible for the nephelometer experiments and data analysis and I took an active part in the discussions regarding the data analysis and interpretation of the results and wrote the paper together with the co-authors.*

### III. **Laser-induced incandescence ( $2\lambda$ and $2C$ ) for estimating absorption efficiency of differently matured soot**

S. Török, Manu Mannazhi, and P-E. Bengtsson

Applied Physics B, 127(7): 96 (2021)

Laser-induced incandescence was used to investigate the absorption wavelength dependence of the refractory part of mini-CAST soot of different maturity. It was shown that for the less mature soot a discrepancy was observed as compared to previous measurements and it was suggested that thermal annealing might influence the results. Therefore caution has to be taken when estimating qualitative information on the absorption properties of less mature soot.

*I planned and performed the experiments and analysed the data. I wrote the paper with help from the co-authors.*

### IV. **Investigating the influence of rapid laser heating of differently matured soot with double-pulse laser-induced incandescence**

S. Török, M. Mannazhi, S. Bergqvist, K.C. Le, and P-E. Bengtsson

Manuscript to be submitted.

An investigation of the influence of rapid laser-heating of differently matured soot for improved understanding of physical processes involved during LII measurements. A double-pulse setup was used with two-color detection for pyrometry and with excitation at two wavelengths allowing for investigation of the wavelength dependence of the involved processes. Results show extensive absorption enhancement and enhanced laser induced fluorescence contribution after laser heating young soot. The work highlights the differences between LII on young and mature soot.

*I planned and performed the experiments. I did the analysis of the data and wrote the paper with the help of Per-Erik Bengtsson and the input from the co-authors.*

# Nomenclature

$a$	Primary particle radius	$P_v$	Partial pressure
$c_p$	Specific heat capacity	$q$	scattering wave vector
$CO_2$	Carbon dioxide	$\dot{q}_{abs}$	Rate of absorption
$D_f$	Fractal dimension	$\dot{q}_{ann}$	Rate of annealing
$d_m$	Mobility diameter	$\dot{q}_{cond}$	Rate of heat conduction
$d_{pp}$	Primary particle diameter	$\dot{q}_{rad}$	Rate of radiation
$E(m)$	Absorption function	$\dot{q}_{sub}$	Rate of sublimation
$E_g$	Optical band gap	$Q$	Integrated forward to backward scattering
$F(m)$	Scattering function	$R$	Molar gas constant
$F_{laser}$	Laser fluence	$R_g$	Radius of gyration
$G(\lambda)$	Scattering intensity function observed by the nephelometer	$S(q)$	Structure factor
$H_2O$	Water	$sp^2$	Hybrid orbital of 1s and 2p orbitals
$I_0$	Incoming light intensity	$T$	Temperature
$I_t$	Transmitted light intensity	$t_{pulse}$	Pulse duration
$k$	Wave vector	$t_{res}$	Residence time
$k$	Imaginary part of the refractive index	$\beta$	Mass accommodation coefficient
$k_0$	Shape factor	$\Delta H_v$	Heat of vaporization
$L$	Extinction cell length	$\varepsilon$	Emissivity
$m$	Complex refractive index	$\theta$	Scattering angle
$MAC$	Mass absorption coefficient	$\lambda$	Wavelength
$m_p$	Particle mass	$\zeta$	Dispersion coefficient
$M_v$	Molecular weight	$\rho$	Density
$n$	Real part of the complex refractive index	$\sigma_{abs}$	Absorption cross section
$N_a$	Number of primary particles per aggregate	$\sigma_{ext}$	Extinction cross section
$N_v$	Molecular flux of carbon fragments	$\sigma_{scat}$	Scattering cross section

$p(t)$	Function of the laser temporal profile	$\varphi$	Equivalence ratio
--------	--	-----------	-------------------

### *Abbreviations and acronyms*

AAE	Absorption Ångström exponent	OA	Organic aerosol
BC	Black carbon	OC	Organic carbon
BP	By-pass	OP	Operation point
BrC	Brown carbon	rBC	refractory black carbon
C/O	Carbon to oxygen ratio	RDG	Rayleigh-Debye-Gans
CAST	Combustion aerosol standard	ROS	Reactive oxygenated species
CPC	Condensation particle counter	RSR	Resonance stabilized radicals
CW	Continuos wave	SAE	Scattering Ångström exponent
DMA	Differential mobility analyzer	SMPS	Scanning mobility particle sizer
eBC	Equivalent black carbon	SOA	Secondary organic aerosol
EC	Elemental carbon	SP2	Single particle soot photometer
ELS	Elastic light scattering	SP-AMS	Soot particle aerosol mass spectrometer
EUSAAR_2	Heating scheme for thermo-optical analysis	TC	Total carbon
FID	Flame ionization detector	TD	Termodenuder
GMD	Geometric mean diameter	TEM	Transmission electron microscopy
HACA	Hydrogen abstraction (or activation) carbon addition	PMT	Photomultiplier tube
HULIS	Humic like substances	PAH	Polycyclic aromatic hydrocarbon
LIF	Laser induced fluorescence	PC	Pyrolytic carbon
LII	Laser induced incandescence		

# Contents

<b>Abstract</b> .....	<b>i</b>
<b>Populärvetenskaplig sammanfattning</b> .....	<b>iii</b>
<b>List of publications</b> .....	<b>v</b>
<b>The author's contributions</b> .....	<b>vii</b>
<b>1 Introduction</b> .....	<b>1</b>
1.1 The implications of soot .....	1
1.2 Soot diagnostics .....	3
1.3 Aims and objectives.....	4
<b>2 Soot</b> .....	<b>5</b>
2.1 Soot formation, evolution and maturation .....	5
2.2 Soot as BC and BrC.....	8
2.3 The mini-CAST .....	9
<b>3 Theory and methods</b> .....	<b>13</b>
3.1 Important quantities for soot characterization .....	13
3.1.1 Optical quantities .....	13
3.1.2 Morphology .....	16
3.2 Optical diagnostics .....	17
3.2.1 Extinction.....	18
3.2.2 Laser-Induced Incandescence (LII) .....	20
3.2.3 Elastic light scattering .....	29
3.3 Aerosol diagnostics.....	32
<b>4 Results</b> .....	<b>35</b>
4.1 Characterization of soot of various maturity and morphology .....	35
4.1.1 Optical and physicochemical properties .....	35
4.1.2 Investigations of soot morphology .....	41
4.2 Soot-laser interaction.....	44
4.2.1 1-pulse experiments .....	44



4.2.2	2-pulse experiments .....	48
4.2.3	Continuous wave LII (CW-LII) .....	53
<b>5</b>	<b>Summary and conclusions .....</b>	<b>55</b>
<b>6</b>	<b>Outlook.....</b>	<b>59</b>
	<b>Bibliography.....</b>	<b>61</b>
	<b>Acknowledgements .....</b>	<b>69</b>

# 1 Introduction

## 1.1 The implications of soot

Combustion has always been the primary technology to provide humanity with energy. But the related accelerating global greenhouse gas emissions (carbon dioxide, methane etc.) is of major concern as it has a negative impact on the climate, on human health and on the environment. Despite the urge to decrease emissions of greenhouse gases to prevent the global temperature from reaching +1.5 °C above the preindustrial temperature to meet the Paris agreement, there are challenges to convert from fossil fuel use to more sustainable and carbon-reduced energy sources.

Soot is formed during incomplete combustion and may be directly emitted into the atmosphere. Due to its excellent ability to absorb solar radiation and convert it to heat, it is one of the most prominent contributors to positive radiative forcing, after carbon dioxide (CO<sub>2</sub>) [1, 2]. Apart from its direct radiative forcing effect, soot may also indirectly influence the radiative balance of the earth by influencing cloud formation in different ways, by depositing on snow and ice and accelerate ice melting, and by changing the surface albedo of the earth [1, 2], see **Figure 1.1**. Nevertheless, as the soot aerosol processes are complex, uncertainties regarding the climate impact of soot are large due to the difficulty of modelling, as well as the knowledge surrounding the distribution and abundance of soot in the atmosphere is limited, and due to the complexity of soot-cloud interaction [1].

Soot in the atmosphere is a pollutant and it is in particular bad for human and animal health as it is co-emitted with species such as e.g. polycyclic aromatic hydrocarbons (PAHs) which to various degrees are carcinogenic, mutagenic and allergenic[3, 4]. And as the particles are of very small size (submicron range), they may penetrate and deposit deep into the alveolar region of the lungs which allows them to cause health damage. There has also been evidence showing that soot and PAHs can trigger reactive oxygen species (ROS) formation, which may cause serious DNA damage [4]. The world health organization (WHO) reports that millions of people die prematurely due to aerosol pollutants such as soot [5].

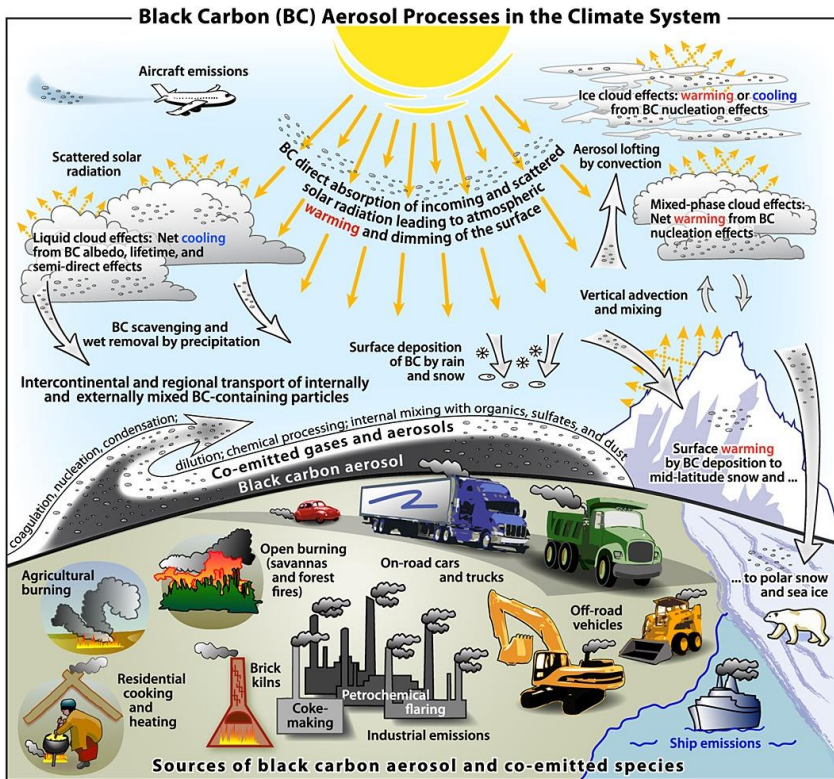


**Figure 1.1.** An overview of the aerosol processes of black carbon (BC; mature soot). The wide variety of natural and anthropogenic sources of BC are shown together with the soot interacting with the environment in terms of radiative forcing effects. [1]

In **Figure 1.1**, an overview is shown of the many different types of soot sources, where open burning (e.g. savannas and forests fires) is the largest soot source as it was estimated to contribute to about 36 % of all emissions during the year 2000 according to inventories discussed in [1]. The emissions from other anthropogenic sources such as diesel engines, industry, and residential solid fuel burning were together responsible for 56 %, with a large regional variation. The final 8 % was assigned to other sources such as e.g. aviation, shipping, and flaring emissions. Soot particles, which are in the size range of tens of nanometers (nm) to a few micrometres ( $\mu\text{m}$ ), may have a lifetime of about a week in the atmosphere (specifically in the troposphere which is at  $\sim 0\text{-}15$  km above the surface) and can cross oceans during that time before it settles or is removed due to precipitation [6]. As soot is considered a short-lived climate forcer due to its relatively short life time in the atmosphere, decreasing soot emissions may be a potential mitigation measure of global warming. Such a mitigation measure could act co-beneficial as soot is also hazardous as a pollutant, and for human health. The climate system is however very

complex and the response to lowered aerosol emissions are very dependent on what type of emission cutting strategy is used [7, 8].

Discussing soot as a climate forcer above and in [1] and [2] does however not show the full picture as it only takes the mature soot into account, namely black carbon (BC). BC is the most mature soot with the most efficient absorption properties, highest density, insoluble, and refractory up to about 4000 K [9]. Depending on the combustion process where the soot was formed, the emitted soot may have properties which deviate from that of BC. Brown carbon (BrC) is a subgroup of light absorbing organic aerosol (OA) which has received increasing attention the past couple of years, as it may be an important contributor to radiative forcing. BrC is a particle type with relatively wide range of properties. They are in the size range of BC, does not absorb light as efficiently as BC, but has a stronger absorption wavelength dependence. BrC is typically formed during biomass or solid fuel combustion, or smouldering fires where the combustion temperatures are not as high as e.g. during typical fossil fuel combustion. BrC particles may be atmospheric organic aerosol with properties similar to humic like substances (HULIS), tar [10] and can also be formed as secondary organic aerosol (SOA) [11, 12]. Hence, also young soot may be considered as combustion BrC, as they absorb weakly to moderately in the visible wavelength range, depending on the soot maturity. BC and BrC together do span over the so called '*brown-black continuum*' of absorbing carbonaceous particles, as shown and discussed in [13].

Increased understanding of the radiative properties of BrC in the atmosphere is crucial as it has been observed that BrC may play an important role as a climate forcer [12, 13], most probably to positive radiative forcing [12].

## 1.2 Soot diagnostics

Optical techniques have long been used to investigate how aerosols interact with light as e.g. done by Anders Ångström during the 1920s when the wavelength dependence of the sunlight attenuation passing through the atmosphere was studied [14]. Since then much has happened in terms of the technical evolution and optical measurement techniques can today provide non-intrusive tools for optical diagnostics of soot both *in-situ* and *ex-situ*.

The absorption and scattering properties of soot is of great interest as to understand how they interact with the radiation from the sun. Techniques such as light extinction (presented in relation to *Paper I*), laser-induced incandescence (LII; used in the works of *Paper III and IV*), photo-acoustic spectroscopy, aethalometer (used in the work of *Paper I*), nephelometer (used in the work of *Paper II*), elastic light scattering (ELS; measured in the work of *Paper IV*) and laser induced fluorescence

(LIF) are non-intrusive techniques which may provide absorption and scattering information of soot. But to obtain a more complete picture of soot and to understand how the optical and physicochemical properties correlate, other types of optical and aerosol techniques can be used to get a more complete picture. Examples of techniques in this category, which were also used in the work presented in this thesis, are thermo-optical analysis (OC/EC analysis), soot particle aerosol mass spectrometer (SP-AMS), scanning mobility particle sizer (SMPS) and transmission electron microscopy (TEM).

It is highly important that the diagnostic tools used can differentiate between the different types of soot accurately as the properties of the soot may vary over a wide range; the brown-black continuum. The techniques used throughout the work presented in this thesis are described in more detail in Section 3.

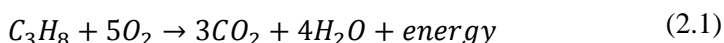
### 1.3 Aims and objectives

As stated by the title of this thesis, the aim of this work was to investigate and characterize the optical and morphological properties of differently matured soot, which was produced from a mini-CAST laboratory soot generator. The specific purpose was to improve the understanding of how soot of various maturity interacts with electromagnetic radiation, and how optical techniques, specifically a nephelometer and LII may be used for quantitative and qualitative measurements of soot depending on its maturity. The objectives of *Paper I-IV* are listed below

- To investigate how the absorption properties of soot is dictated by its physicochemical properties, and specifically how the properties are related to the refractory and non-refractory constituents of the soot. (*Paper I*)
- To investigate if a commercial 3-wavelength nephelometer can be used in combination with RDG-theory to obtain morphological properties of soot and potentially information on the maturity of soot particles in aerosol phase. (*Paper II*)
- To understand how laser-induced incandescence may be used for investigations of absorption properties of young soot as well as mature soot, and in relation to extinction measurements (*Paper III*)
- Investigating how rapid laser heating of soot of different maturity influences the soot. (*Paper IV*)

## 2 Soot

Combustion can be described as an exothermic reaction between a fuel and oxidizer, as for example shown in Equation 2.1 for propane ( $C_3H_8$ ), a hydrocarbon fuel which has been used throughout the work presented in this thesis.



Equation 2.1 shows the global equation of a stoichiometric mixture of propane and oxygen, meaning that the constituents are balanced to provide complete combustion with carbon dioxide ( $CO_2$ ) and water ( $H_2O$ ) as the only products<sup>1</sup>. In real combustion systems, the balance between the amount of fuel and oxidizer may however vary in time and space, resulting in products which are not only carbon dioxide and water. When there is an excess of fuel (rich mixture), the oxidizer will not be sufficient to oxidize all the intermediate carbon species formed and hence the combustion will be *incomplete*. Under such rich combustion conditions, with a sufficiently high C/O-ratio (carbon to oxygen ratio) and high temperatures, carbonaceous material termed *soot* may form.

### 2.1 Soot formation, evolution and maturation

The formation of soot in a combustion environment is a highly complex process. As the hydrocarbon fuel has undergone pyrolysis, precursor molecules, e.g. polycyclic aromatic hydrocarbons (PAHs), may be formed if the environment is carbon-rich. Despite challenges in understanding certain parts of soot formation, there is a general consensus that PAHs are the main precursors of soot [15-17]. As PAH molecules will grow bigger and get arranged into stacked units, they may eventually condense into incipient soot particles. When the large molecular structure of PAHs condenses, it is the point of soot inception, see **Figure 2.1** where inception occurs

---

<sup>1</sup> It should however be noted that the oxidation process of the fuel is very complex. There will be many elementary reactions on the path of the combustion process which involves the formation of intermediate species. Also the chemical equilibrium concentrations will be highly dependent on temperature.

between **a** and **b**. The molecular growth in a hot combustion environment, where small precursor molecules successively grow to aromatic structures of increasing size, polycyclic aromatic hydrocarbons (PAHs), and eventually incipient soot, has however puzzled researchers for a long time and the kinetic-thermodynamic coupling of the pathways to PAH formation does not always end up favourable [15]. Nevertheless, progress has been made, as different mechanisms and pathways have been suggested, see [15, 16] and references therein. The widely accepted *HACA* mechanism (hydrogen abstraction or “*activated*” [16] carbon addition) describes molecular growth by a repetitive addition of acetylene (the most abundant growth species in combustion) to a hydrogen abstracted (and re-activated) growing PAH. Another pathway to PAH growth in flames was presented recently by Johansson et al. [18] who proposed radical-chain reaction by resonance stabilized radicals (RSR) as a possible pathway to soot formation [18], where larger re-activated RSRs may grow by reaction with other hydrocarbon species, forming covalently bonded complexes, contributing to particle surface growth. Frenklach et al. [16] however critically points out that more work is needed to fully understand the growth of smaller aromatics in [18]. Further, a *HACA*-driven mechanism was proposed in [16] where dimer formation from interaction between an aromatic molecule and an aromatic radical as they may remain an adduct long enough (due to rotational activity upon collision) to form covalent bonds, even for small and moderately sized PAHs [16]. As experimental evidence also points at presence of dimers in the nucleation region of premixed flames [19, 20], dimerization may be an important mechanism leading to the formation of the first condensed incipient soot particle [16, 21]. Nevertheless more work is needed on the matter to further explore and validate the suggested mechanism.

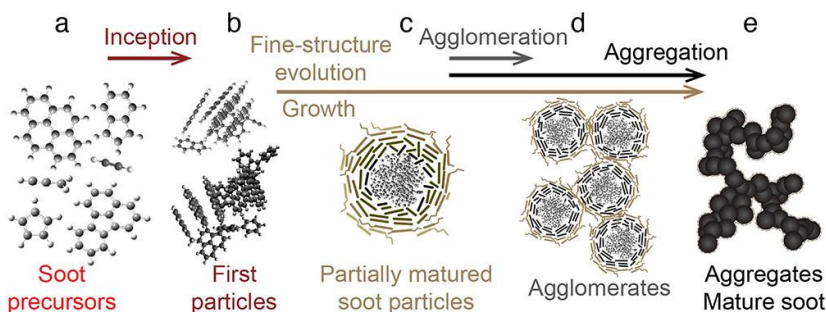


**Figure 2.1.** In a) PAHs and acetylene, the important precursors and growth species involved during the gas-phase reaction leading to soot inception. As the growth of stacked PAHs has allowed for soot inception, the first particles are formed, see b). These will coalesce, further grow to obtain a graphitic outer layer and get carbonized, to form partially matured soot particles see c). The partially matured soot will form agglomerates d) and as the soot further spend time in the hot environment, further carbonization, graphitization, and growth will result in mature soot aggregates as seen in e). Reprinted with permission from [22]. Copyright 2020 American Chemical Society.

As an incipient soot particle is formed, it will further evolve during its life time in the combustion environment. The evolution of the soot will be described as presented in [22, 23]. Incipient soot particles can be considered as condensed aromatic hydrocarbons, in the size range of about 1-6 nm but as the particles may grow through surface growth and by coalescence with other particles, it will form larger primary soot particles. Soot particles will start to coagulate and form agglomerates where the primary particles are loosely bound (by Van der Waals forces), to further mature and form stronger covalent bonds between the primary particles and become rigid aggregates (see a typical ramified soot aggregate in **Figure 2.2**). As the particles mature, de-hydrogenation will make the amorphous soot more carbonized and also becoming of increased graphitic character. This leads to an increased C/H ratio from  $\sim 2$  (for incipient soot) up to about 10-20, and an increased  $sp^2/sp^3$  ratio of the carbon atoms as the soot becomes more ordered with larger aromatic units arranged along the direction of the soot surface.

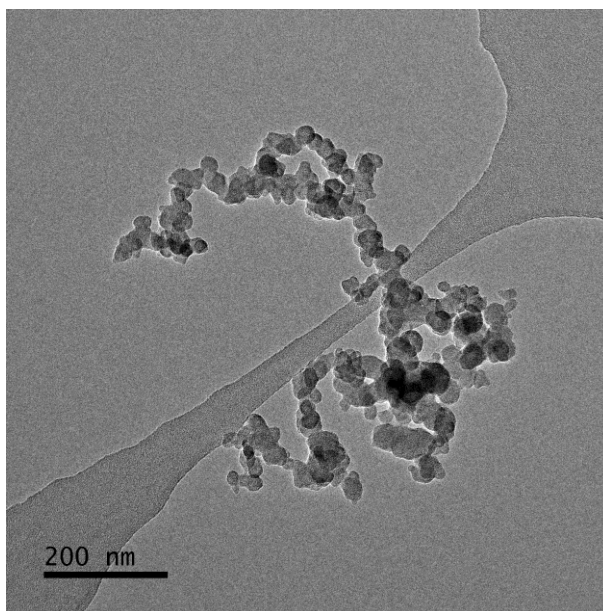


**Figure 2.2.** A mature mini-CAST soot aggregate imaged using transmission electron microscopy (TEM).

As the soot matures, there will be a subsequent change in the optical properties of the soot. Incipient particles may appear transparent, but along the path of maturation, the soot nanostructure becomes more ordered and hence there will be an increased amount of delocalized electrons which will result in a more efficient light absorption. And with the absorption efficiency, the absorption wavelength dependence of the soot will also evolve. Hence, the optical properties may range



from close to transparent, to brown-colored and finally black for mature soot. In **Figure 2.3**, an overview is given showing the change of soot properties as it matures (along the brown-black continuum). A description of the optical quantities in **Figure 2.3** will be described in detail in Section 3.1.

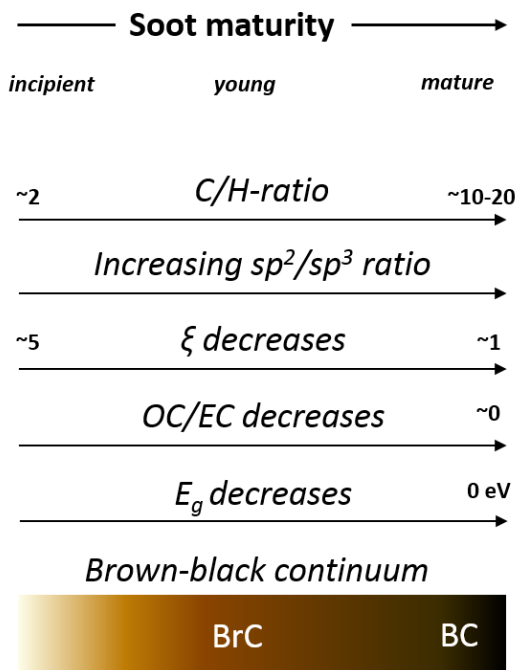


**Figure 2.3.** As soot is formed, it will evolve during its time in the combustion. As it matures, its properties will change due to growth, change and as the composition and the structure of it will change. The subsequent change of properties in relation to the maturation is shown. The brown-black continuum is divided into the mature soot as black carbon BC while the not yet matured soot can be considered as brown carbon BrC.

## 2.2 Soot as BC and BrC

Light absorbing particles originating from combustion emitted into the atmosphere may be divided into black carbon (BC) and brown carbon (BrC) depending on its optical properties, as discussed in the introduction [1].

BC is as previously discussed defined as mature soot, which is emitted into the atmosphere after it has been formed in combustion. BrC is however not as well defined as BC, as its origin, composition and hence its optical properties may vary [11, 13]. BrC is as the name suggests, less absorbing aerosol which is often co-

emitted with BC, but may also be formed in the atmosphere as secondary aerosol [11, 24]. As discussed in *Paper I* and presented by Saleh et al. [13], young soot which has not yet matured will appear brown and have a strong absorption wavelength dependence which agree with the criterion for BrC. Hence, as discussed by Saleh et al. [13], there is a brown-black continuum of light absorbing aerosol particles (see representation in **Figure 2.3**) which span from the weakly absorbing BrC, to strongly absorbing BrC and to BC, where soot of different maturity can span over the whole spectrum (as illustrated in **Figure 2.3**).

## 2.3 The mini-CAST

Soot generators in terms of soot standard for calibration purposes has attained large interest in the field of emission regulations (e.g. for diesel engines and turbine engines) [25-29]. But in the work presented in this thesis, a miniature combustion aerosol standard (mini-CAST) model 5201C (see **Figure 2.4a**) manufactured by Jing Ltd [30] is the target soot source for the purpose of generation of differently matured soot. The mini-CAST operates on a propane-air co-flow diffusion flame, which is quenched at a fixed height above the burner, see schematics in **b**, where the flame and all the gas flows are indicated.

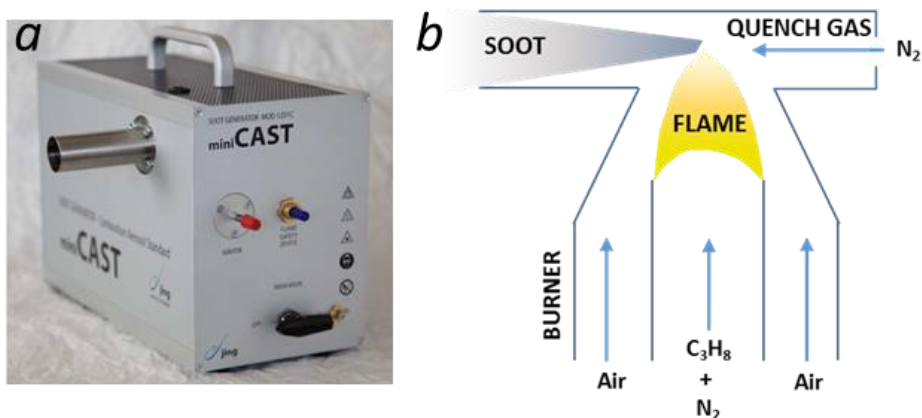


**Figure 2.4.** In a) an image of the mini-CAST 5201c is shown. The schematics of the mini-CAST burner is shown in b) where the fuel mix (propane with/without N<sub>2</sub>) and co-flow air is introduced in the burner. As the flame is stabilized on the burner, a high N<sub>2</sub> flow will quench the flame from the side at a fixed height to cool the soot formation process and emit cold soot particles. The possibility of further air dilution can be introduced but is not included in the schematics.

The properties of the emitted soot, will hence depend on the evolution of the soot formation process in the flame. By changing the properties of the flame, different types of soot particles may be emitted from the mini-CAST. The characteristics of the diffusion flame can be changed by 1) changing the global equivalence ratio ( $\Phi_{\text{global}}$ ), 2) changing the overall gas flow (denoted ‘*Total flow*’ in **Table 2.1**) and 3) by diluting the flame with an inert gas, in our case nitrogen ( $\text{N}_2$ ). In **Table 2.1**, all the settings are shown for the investigated soot types, OP1-8. It is shown that with increasing OP number, the nitrogen flow is increased, the global equivalence ratio is increased, and the total flow is increased.

**Table 2.1.** The operation points (OP) used for the mini-CAST to produce the different types of mini-CAST soot. All the flows are given as standard litres per minute (slpm). The global equivalence ratio and the fuel ratio is included for discussion related to the differences in flame properties.

	Air slpm	Propane slpm	$\text{N}_2$ lpm	Quench slpm	Total flow slpm	$\Phi_{\text{global}}$	$X_{\text{fuel}}$ (%)
<b>OP1</b>	1.55	0.06	0	7	1.61	0.9217	100
OP2	1.54	0.06	0.050	7	1.65	0.9276	54.5
<b>OP3</b>	1.52	0.06	0.100	7	1.68	0.9398	37.5
OP4	1.50	0.06	0.150	7	1.71	0.9524	28.6
<b>OP5</b>	1.47	0.06	0.200	7	1.73	0.9718	23.1
<b>OP6</b>	1.42	0.06	0.250	7	1.73	1.0060	19.4
<b>OP7</b>	1.36	0.06	0.300	7	1.72	1.0504	16.7
OP8	1.32	0.06	0.330	7	1.71	1.0823	15.4

Nitrogen dilution is a well explored method for altering the soot formation [31], as combustion temperature and the dilution of the fuel will influence the soot formation process. An increased dilution with  $\text{N}_2$  has been shown to decrease the flame height [31, 32], increase the visible flame height position at which soot formation starts [32] and a decrease of the overall soot volume fraction [31, 32]. Hence, for the different mini-CAST operation points (OP) used in the presented work, enhanced  $\text{N}_2$ -dilution will essentially result in quenching soot from earlier on in the soot formation process. In **Figure 2.5** an attempt is done to visualize how the flame appearance will change and how the quenched region will correspond to a region closer to the early soot formation.

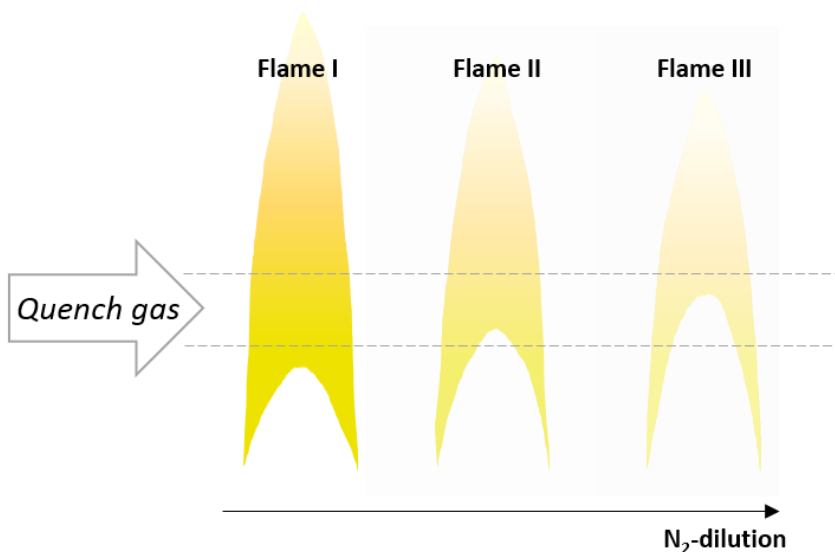


**Figure 2.5.** Three simplified diffusion flames are shown with different amount of N<sub>2</sub>-dilution. With increasing amount of dilution it can be seen that the visible flame height increases, flame height decreases and the soot abundance decreases. This is a simplified approach where the differences in soot concentration and soot properties are neglected.

The properties of the soot produced by the mini-CAST will vary in terms of shape, size and composition (chemical and structural), which will in turn influence the soot optical properties as discussed in Section 2.1. In **Figure 2.6**, mini-CAST soot sampled on glass is shown for 5 different OP cases. Despite the differences in soot concentration on the glass, different colours of the soot can be observed, which can be related to the differences in absorption properties of the different types of soot.



**Figure 2.6.** Sampled mini-CAST soot on a small sapphire glass. As can be seen, the colour appears different of the various soot types as the OP1 and OP3 soot is black, while the sampled OP5-7 soot gives a more brownish and yellow colour. Note that the collected mass varies between the samples and may hence influence the true relative colour. With courtesy of Thi Kim Cuong.

In the work performed in *Paper I*, the OP1, OP3, and OP5-7 soot was investigated to get a broad distribution of soot properties investigated. In *Paper II* all types of soot (OP1-OP8) are used and in *Paper III* and *IV*, the work is focused on OP1, OP6 and OP7 soot.

# 3 Theory and methods

## 3.1 Important quantities for soot characterization

The optical and morphological properties of soot will dictate the scattering and absorption properties of soot. Hence, well-planned optical measurements may be done to obtain information about various soot properties. In this section, a few quantities will be reviewed which are of importance for the work presented in this thesis. Discussion on optical properties is mainly based on the theory presented in [33, 34].

### 3.1.1 Optical quantities

The **complex refractive index**  $m$  for a medium describes its interaction with electromagnetic radiation, and can be given by

$$m = n - ik, \quad (3.1)$$

where the imaginary part of the complex refractive index  $k$  describes the attenuation of electromagnetic radiation while the real  $n$  describes the phase velocity,  $v=c/n$ . The complex refractive index is a function dependent on wavelength and the real and imaginary parts are related through the Kramer-Kronig relations [33, 35], allowing for estimations of  $m$  by e.g. absorption measurements [36]. Values of  $m$  for soot have been reported in the literature, and according to a recent review by Liu et al. [37], the range given for mature soot is suggested to be  $1.5 < n < 1.86$  and  $0.68 < k < 1$  (at 550 nm), while for brown carbon  $k$  may range over two orders of magnitude [13, 38].

Soot particles consists of primary particles which are much smaller than the wavelength and are in the **Rayleigh regime** ( $\pi d_{pp}/\lambda \ll 1$ ). The **absorption coefficient**  $\sigma_{abs}$ , is hence defined for a primary particle as follows,

$$\sigma_{abs} = \frac{\pi^2 d_{pp}^3 E(m)}{\lambda}, \quad (3.2)$$

where  $d_{pp}$  is the primary particle diameter and  $E(m)$  is the **absorption function**, which is defined by

$$E(m) = -Im \left( \frac{m^2-1}{m^2+2} \right), \quad (3.3)$$

according to [33]. Hence, both the real and the imaginary part of the complex refractive index will influence the absorption properties of soot.  $E(m)$  is also to some extent wavelength dependent, which will be discussed throughout the thesis. As given by the real and imaginary part of the complex refractive index,  $E(m)$  would fall in the range of 0.32-0.4 at 550 nm [37] and decrease with decreasing soot maturity. It has however been shown that not only maturity in terms of bulk material, but also the primary particle size does have an impact on the optical properties. If they are small enough, in the range of  $< 15$  nm, soot particles may have a quantum dot behaviour with an increasing optical band gap for decreasing particle sizes [36, 39], which in turn means lower absorption.

In the same manner as for absorption, the scattering cross section is linearly proportional to a  $m$ -dependent function, namely the **scattering function**  $F(m)$ , which is expressed as follows.

$$F(m) = \left| \frac{m^2-1}{m^2+2} \right|^2 \quad (3.4)$$

The  $E(m)$  and  $F(m)$  dependence on  $m$  and in relation to each other is shown in the contour plot in **Figure 3.1**, where also the region of plausible values of  $m$  for mature soot is marked according to suggestions in [37]. It should however be noted that there are many estimations and suggestions of  $m$  for soot in the literature as e.g. [40, 41], and as pointed out in [37], there is still a need for controlled experiments to be done in order to perform accurate estimations of  $m$  for mature soot.

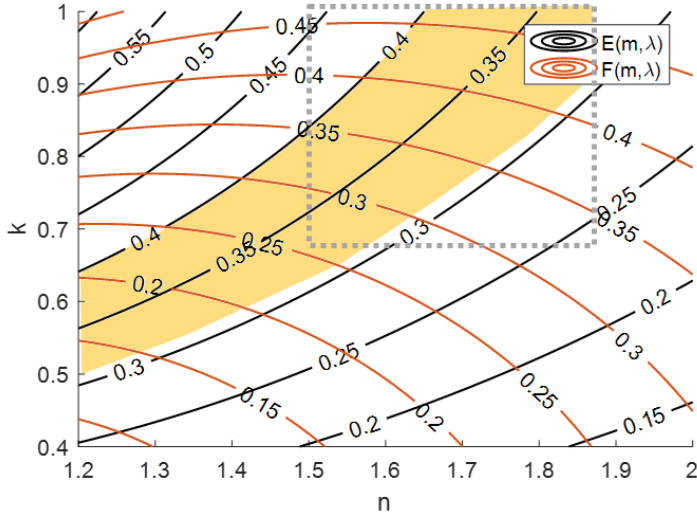


**Figure 3.1.** Contour plot of  $E(m)$  and  $F(m)$ . The suggested values for mature soot are  $E(m)=0.32-0.4$  (the yellow marked region) and  $1.5 < n < 1.86$  and  $0.68 < k < 1$  (at 550 nm) (the gray dashed box) according to [37].

In the aerosol community, the **mass absorption cross section (MAC)** is often utilized for the description of the absorption properties of absorbing aerosols and it is considered an important parameter for climate modelling purposes [1]. It is also used to convert between absorption and aerosol mass when using absorption techniques. MAC is defined according to

$$MAC = \frac{\sigma_{abs}}{m_p}, \quad (3.5)$$

where  $m_p$  is the aerosol particle mass. According to the well cited review by Bond et al. [42] a MAC value of  $7.5 \pm 1.2 \text{ m}^2/\text{g}$  was suggested for BC, but according to more recent observations, this value was considered somewhat too low as  $8 \pm 0.7 \text{ m}^2/\text{g}$  was suggested by [37]. Brown carbon however absorbs light more poorly and may have a lower MAC related to the position in the brown-black continuum [13].

Another physical quantity which can be useful to characterize the optical properties of soot and which may be related to the maturity of soot is the **dispersion coefficient**  $\xi$ , often also termed the **absorption Ångström exponent (AAE)** in the aerosol community and in *Paper I* [14]. It describes the absorption wavelength dependence and can be related to the absorption coefficient  $\sigma_{abs}$  and the absorption wavelength  $\lambda_x$  according to



$$\xi = \frac{\log(\sigma_{abs}(\lambda_1)/\sigma_{abs}(\lambda_2))}{\log(\lambda_1/\lambda_2)}, \quad (3.6)$$

where  $\xi$  will be specific for the wavelength pair ( $\lambda_1$  and  $\lambda_2$ ). The dispersion coefficient has a value close to 1 for mature soot, while the value increases the less mature the soot is. Observations have shown values as high as  $\sim 3.5$  for young mini-CAST soot and  $\sim 4$  at low heights above burner in a premixed ethylene-air flame, as shown in *Paper I* and in [43].

An optical parameter which is related to the dispersion coefficient is the **optical band-gap**  $E_g$ . It describes the absorption properties of soot in terms of the lowest possible energy of photon absorption.  $E_g$  decreases with an increasing order of the soot (increasing  $sp^2$  content), as larger graphitic layers will give rise to a larger amount of conjugated  $\pi$ -electrons allowing absorption at longer wavelengths [44, 45].

### 3.1.2 Morphology

Soot aggregates have a fractal-like shape, which can be described by the following fractal law [34, 46],

$$N_a = k_0 \left( \frac{R_g}{a} \right)^{D_f}, \quad (3.7)$$

where  $N_a$  is the number of primary particles,  $k_0$  is the fractal pre-factor,  $R_g$  is the radius of gyration,  $a$  is the primary particle radius, and  $D_f$  is the fractal dimension of the aggregate. In **Figure 3.2**, an example of a soot aggregate is shown with  $R_g$  and  $a$  marked, sampled from the mini-CAST OP1 case. It should be kept in mind, that the fractal law given by Equation 3.7, is a valid description only if there is a large number of primary particles in the aggregate.

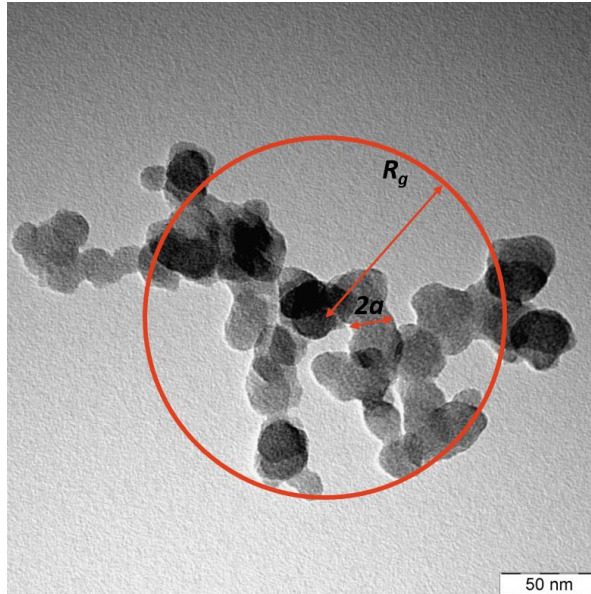


**Figure 3.2.** Transmission electron microscopy (TEM) image of a mini-CAST OP1 soot aggregate.  $D_f = 1.8$ ,  $R_g = 93$  nm,  $a_{\text{mean}} = 22$  nm. Courtesy to Adrian Roth for the TEM image.

The radius of gyration, which essentially describes the soot size, may vary from tens of nanometers for young soot early in the soot formation process to micrometers for large aggregates from combustion where the soot has had the conditions and time to grow and coagulate. The number of primary particles per aggregate will scale accordingly. Primary particle sizes can also range from a few nanometer to tens of nanometers depending on the type of combustion. The fractal dimension of soot depends on combustion source and on analysis method as discussed in [47], but is typically just below  $\sim 2$ . It can however change due to re-structuring as soot ages in the atmosphere. The fractal pre-factor  $k_0$  is additionally a complex parameter which is related to the compactness of the soot [47] as primary particles may overlap and e.g. show bridging features.

## 3.2 Optical diagnostics

Optical techniques for diagnostic purposes are of great importance as they may allow for non-intrusive measurements, often even *in-situ* if optical access is available. In the work presented here, different optical measurement techniques are used to study the optical properties of soot and its response to rapid laser heating. These techniques will be described and discussed in the following sections, specifically focusing on their use for soot diagnostics.

## 3.2.1 Extinction

### 3.2.1.1 Theory

Extinction can be described as the attenuation of light due to absorption and scattering as the light propagates through a medium, see **Figure 3.3**. The attenuation can be described by the Beer-Lambert law, see Equation 3.8, where the transmitted light intensity  $I_t$  through a medium depends on the incident light intensity  $I_0$ , the medium extinction coefficient  $\sigma_{ext}$  and length of the medium  $L$ .

$$I_t = I_0 e^{-\sigma_{ext} L} \quad (3.8)$$

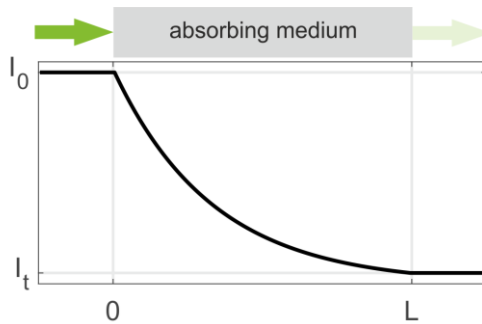


**Figure 3.3.** The illustration shows the attenuation of light through an attenuating medium. The incoming light intensity decreases to the transmitted light intensity level after passing the medium of length  $L$ .

As the extinction is due to the combined effects of absorption and scattering, the extinction coefficient can be described by Equation 3.9,

$$\sigma_{ext} = \sigma_{abs} + \sigma_{scat} \quad (3.9)$$

where  $\sigma_{abs}$  is the absorption coefficient and  $\sigma_{scat}$  is the scattering coefficient.

Soot aggregates in flames are generally considered to fulfil the Rayleigh criterion [34] as the soot particles have a ramified structure of relatively low fractal dimension ( $\sim 1.7-1.9$ , see [41, 48] and references therein) approximately consisting of isotropic and spherical primary particles much smaller than the wavelength  $d_{pp} \ll \lambda$ . Hence, extinction measurements can be utilized for absorption measurements of soot, as  $\sigma_{ext} \approx \sigma_{abs}$ . The definition of the absorption coefficient for soot is given by Rayleigh theory for isotropic spheres according to Equation 3.2 in Section 3.1.1. The absorption coefficient is as shown a function of the absorption function  $E(m)$ , as shown in Equation 3.3 which describes how efficiently the soot absorbs light of a certain wavelength  $\lambda$ .

For mature soot the  $1/\lambda$  relationship given in Equation 3.2 is a valid approximation for  $\sigma_{abs}$  in the visible and near infrared wavelength region, which thereby implies a constant  $E(m)$  [33]. For younger soot, however,  $E(m)$  has been found to have a stronger wavelength dependence [40, 49] and hence  $\sigma_{abs}$  will deviate from the  $1/\lambda$  relationship. To allow for description of the wavelength dependence, a dispersion coefficient  $\zeta$  is defined in Equation 3.6, expressing the relationship  $\sigma_{abs} \propto 1/\lambda^\zeta$ . Equations 3.2 and 3.6 can be combined to obtain the relationship given in Equation 3.10.

$$\frac{E(m, \lambda_1)}{E(m, \lambda_2)} = \left(\frac{\lambda_1}{\lambda_2}\right)^{1-\zeta} \quad (3.10)$$

Hence,  $\zeta$  expresses the wavelength dependence of the absorption efficiency  $E(m)$ .

### 3.2.1.2 Methods

In the work presented in *Paper I*, a multi-wavelength extinction setup was used for measuring the dispersion coefficient, or as named in the paper *Absorption Ångström Exponent (AAE)*. By measuring the attenuation of light at multiple wavelengths through a sooty probe volume, the wavelength dependence of  $\sigma_{abs}$  and hence the dispersion coefficient  $\zeta$  could be obtained.

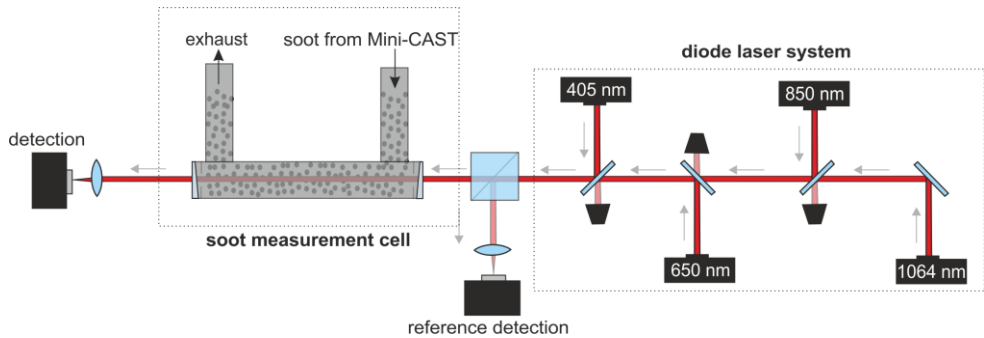


**Figure 3.4.** The experimental setup of the multi- $\lambda$  extinction system used in the work of *Paper I* for investigation of the absorption wavelength dependence.

In **Figure 3.4** a schematic view of the optical setup, used in the work presented in *Paper I*, is shown. The soot aerosol was led through an extinction cell of adjustable length (max length of 20 cm). Two wedged windows allowed optical access in the cell and had a  $N_2$  purge flow onto the windows preventing soot from depositing. The optical path of 4 diode laser beams (405, 650, 850 and 1064 nm) are overlapped by 4 dichroic mirrors to provide extinction measurements in the same probe volume. The beam is split by a beam-splitting cube to allow for a reference beam to be monitored in order to account for laser intensity variations. The measurement beam

is then passed through the extinction cell containing the soot aerosol. Detection of the reference and measurement beam is done using two photodiodes. The laser beam was modulated at 100 Hz and the sampling frequency was 300 kHz, allowing temporally high-resolution monitoring of the extinction and simultaneous background subtraction. The system was originally developed for usage in applied environments where combustion may be turbulent, hence motivating the high temporal resolution of the detection system.

### 3.2.2 Laser-Induced Incandescence (LII)

The principle of laser-induced incandescence, is as the name suggests, heating the soot to high temperatures ( $\sim 3000\text{-}4000$  K) with a high power laser pulse leading to stronger thermal radiation, i.e. incandescence [48, 50, 51]. As soot is exposed to a short laser-pulse, it will absorb energy during the time of the pulse, but many other processes will occur during and after the pulse which will influence the soot temperature. The energy balance equation of laser-heated soot describes the change in the internal energy  $dU_{int}/dt$  as a function of the different physical processes involved, see Equation 3.11 where the main processes are included.

$$\frac{dU_{int}}{dt} = \dot{q}_{abs} + \dot{q}_{cond} + \dot{q}_{sub} + \dot{q}_{rad} + \dot{q}_{ann} \quad (3.11)$$

Here,  $\dot{q}_{abs}$  denotes the rate of absorption,  $\dot{q}_{cond}$  is the rate of heat conduction,  $\dot{q}_{sub}$  is the rate of sublimation,  $\dot{q}_{rad}$  is the rate of thermal radiation and  $\dot{q}_{ann}$  is the rate of thermal annealing.

The different processes involved during LII, included in Equation 3.11 and depicted in **Figure 3.5** will be discussed below in terms of physical processes influencing the soot, but also explained by the rate equations used in the LII model which is a useful tool both for understanding LII but also for modelling purposes. The LII model will be further discussed in Section 3.2.2.9.

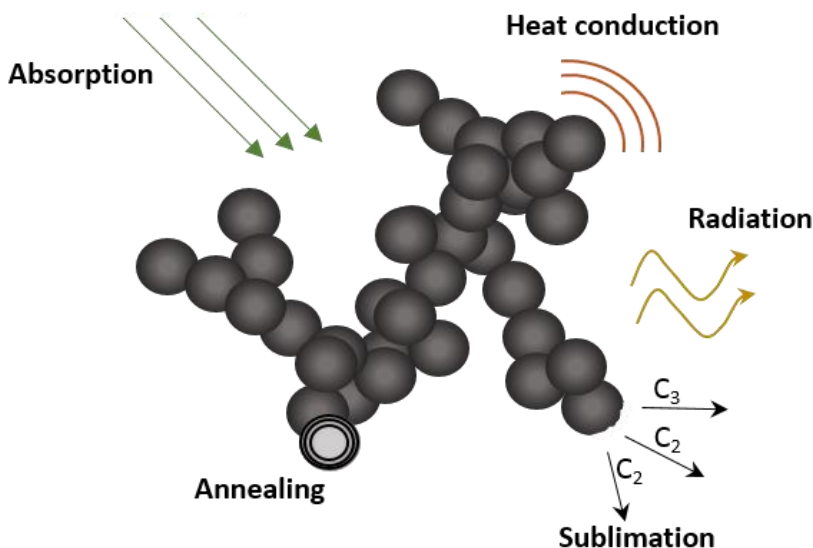


**Figure 3.5.** The illustration shows a soot aggregate and the main physical mechanisms involved during LII measurements. The details regarding the different processes will be discussed in the following sections. The figure is inspired by Figure 7 in [48].

### 3.2.2.1 Internal energy

The change of the internal energy of a primary particle can be described by

$$\frac{dU_{int}}{dt} = \frac{\pi}{6} d_{pp}^3 \rho c_p \frac{dT}{dt}, \quad (3.12)$$

and as can be seen, the volumetric heat capacity  $\rho c_p$  will govern the rate of temperature evolution of the soot. Information about  $\rho c_p$  is useful in estimations of absorption efficiencies, where experimentally a specific amount of energy is absorbed by the soot and the temperature increase is measured. In **Figure 3.6**, the temperature dependence of  $\rho c_p$  is shown. As can be seen it is especially important to take this temperature dependence into account for measurements done on cold soot, while for measurements done in flames, an assumed constant volumetric heat capacity would not induce as large errors. The volumetric heat capacity  $\rho c_p$  has in a recent study been found to be roughly independent of soot maturity [52].

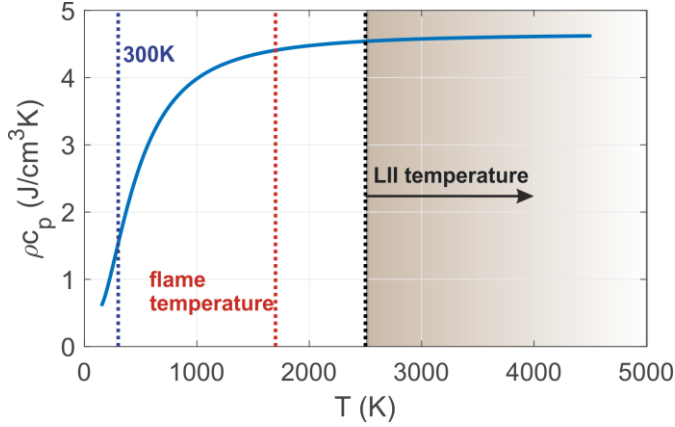


**Figure 3.6.** The blue curve shows the volumetric heat capacity  $\rho c_p$  as a function of temperature ( $T$ ) according to expression from [52]. Room temperature (300 K), a typical flame temperature ( $\sim 1700$  K) and LII temperatures ( $>2500$  K) are marked in the figure to illustrate the different temperature regimes.

### 3.2.2.2 Radiation

As the temperature of soot increases, its emitted thermal radiation will be shifted to lower wavelengths and increase in intensity according to the Planck radiation law. The radiation will however deviate from perfect black body radiation, and this deviation may be described by the soot emissivity  $\varepsilon$ , according to Equation 3.13 [51].

$$\varepsilon = \frac{4\pi d_{pp}^3 E(m)}{\lambda} \quad (3.13)$$

The influence of this radiation term on the energy balance of the soot is however not significant as the term is orders of magnitudes lower than the other processes. Despite this low importance as a heat loss process, this emitted thermal radiation is the LII signal that is detected. The radiation can be used for pyrometry, for example using the ratio of the radiation intensity at two different wavelengths, so-called two-colour pyrometry. Uncertainties in the wavelength dependence of  $E(m)$  leads to uncertainties in the estimated temperature.

### 3.2.2.3 Absorption

The rate of absorption can be described by

$$\dot{q}_{abs} = \frac{\pi^2 d_{pp}^3 E(m)}{\lambda} p(t), \quad (3.14)$$

where  $p(t)$  is the temporal intensity profile of the laser pulse [51]. Hence, the rate of absorption will depend on the absorption efficiency (given by  $E(m)$ ), the temporal laser profile and the soot volume given by  $d_{pp}^3$ , as the soot primary particles are small enough to be considered volume absorbers.

In the energy regime where sublimation is not significant and absorption is the dominant term in Equation 3.11, the absorbed energy will be independent of the temporal laser intensity profile and hence Equation 3.14 can be reformulated to

$$\dot{q}_{abs} = \frac{\pi^2 d_{pp}^3 E(m)}{\lambda} F_{laser}, \quad (3.15)$$

where  $F_{laser}$  is the laser fluence given by  $F_{laser} = \int_0^{t^{pulse}} p(t) dt$ . It is convenient to express the rate of absorption as a function of the fluence, as the fluence can be monitored during experiments based on measurements of pulse energy and cross sectional area.

By combining Equation 3.12 and 3.15, neglecting time dependence, and assuming only absorption influencing the soot temperature, one may obtain an expression for estimating  $E(m)$ , in the absorption-dominated fluence regime. From temperature vs fluence curves,  $E(m)$  can be obtained by

$$E(m) = \frac{\lambda \rho c_p}{6\pi} \frac{\Delta T}{\Delta F_{laser}}, \quad (3.16)$$

where  $\Delta F_{laser}$  is the energy needed to heat the soot a temperature difference of  $\Delta T$ , which is the difference in temperature in a region where the volumetric heat capacity  $\rho c_p$  is approximately constant. By assuming that  $E(m)$  has a constant value during the heating, Equation 3.16 suggests that the temperature evolution in this regime is linear, which has indeed been observed experimentally [53].

#### 3.2.2.4 Sublimation

As soot is heated to high temperatures (3200 K and higher), extensive mass loss will occur and influence the energy balance of soot both due to energy loss and mass loss. The temperatures at which sublimation occurs, have been shown to partly be related to the maturity of soot, as e.g. showed in [54] where the sublimation threshold was observed to range from 3100 K at low heights above burner for young soot, to 3400 K at higher heights above the burner where the soot was more mature. Experiments have also shown that the aggregate structure remained intact as soot was heated to sublimation temperatures, indicating mass loss from the surface of the soot but no disaggregation [55]. The evaporated carbon fragment may then nucleate and form new particles which has been observed by [55-57].



To understand the mechanisms of sublimation, we consider the LII model, and the description of the rate equation of sublimation. The energy rate of sublimations is described by

$$\dot{q}_{sub} = -\frac{\Delta H_v}{M_v} \frac{dM}{dt}, \quad (3.17)$$

where  $H_v$  is the enthalpy of formation of the carbon clusters,  $M_v$  is its molecular weight and  $dM/dt$  is the mass rate given by

$$\frac{dM}{dt} = -\pi d_{pp}^2 N_v \frac{M_v}{N_A}. \quad (3.18)$$

$N_v$  is the molecular flux of the carbon fragments. From Equation 3.17 it can be seen that the energy loss due to sublimation will depend on how much energy is needed to vaporize certain carbon fragments. The expression for the molecular flux away from the surface, which determines the amount of carbon fragments vaporizing, will be the factor that steers the mass loss rate as shown in Equation 3.18.

For ambient conditions, the simplified expression for the molecular flux can be utilized according to [58] as

$$N_v = -\pi d_{pp}^2 P_v \beta \sqrt{\frac{M_v}{2\pi RT}}, \quad (3.19)$$

where the mass accommodation coefficient  $\beta$  describes the efficiency of sublimation, and  $P_v$  is the partial pressure of the evaporated species.

$P_v$ ,  $M_v$ , and  $\Delta H_v$  are all temperature-dependent functions. These are expressed in [59], and based on the thermodynamic data by Leider et al. [60], as a mean value of carbon clusters  $C_{1-7}$ .

### 3.2.2.5 Heat conduction

Heat conduction is the most important heat loss mechanism in the low fluence regime. As soot is heated to temperatures higher than the surrounding gas, energy will be transmitted from the surface of the soot to the colliding gas molecules. The heat conduction loss is related to the surface-to-volume ratio of the particles, the temperature difference between the particle and the ambient gas ( $\Delta T$ ), and the efficiency of the energy exchange  $\alpha_T$ , which is termed the thermal accommodation coefficient.

An accurate estimation of the influence of heat conduction involves accounting for the aggregate shape, or more specifically shielding [61], overlapping of primary

particles (also called necking or bridging) [62] and reshaping (collapsing of aggregate) [63]. Maturity may also influence heat conduction, as the surface character might influence the efficiency of the heat transfer to the surrounding gas, see [48] and references therein.

### 3.2.2.6 Annealing

As soot is heated to LII temperatures, an enhanced level of structural order may occur as graphitic edge sites may be terminated and form longer graphitic layers. As observed in [64-67] and showed in **Figure 3.7**, rapid laser heating may form so called onion rings with hollow cores or multifaceted rosette structures, depending on the amount of heating and on the original soot structure. Apart from being an exothermic reaction and influencing the soot temperature during LII measurements, annealing alters the soot and may influence its optical and thermodynamic properties.

It is however to the authors knowledge, not clear at this time at which time frame this restructuring occurs. However, as stated in [57], the short time frame of a rapid laser pulse may be limiting and full restructuring cannot be expected.

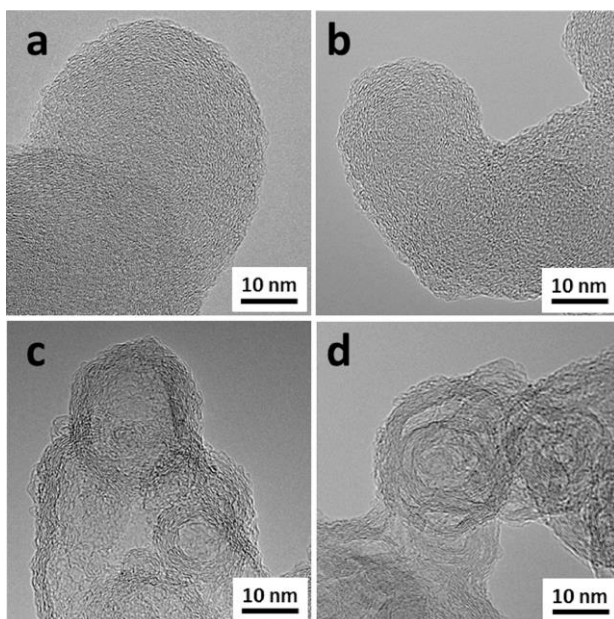


**Figure 3.7.** In the work by [67] young and mature ethylene flame soot was laser heated. **a** and **b** shows the untreated soot, while **c** and **d** show the laser heated soot. The laser heated soot shows extensive structural changes as an enhanced order of long graphitic layers are observed in **c** and multifaceted rosette structures in **d**. Reprinted from [67] with permission from Elsevier.

### 3.2.2.7 LII signal

In **Figure 3.8 a** and **b** two typical modelled LII signals are shown along with the laser pulse used to heat the soot. In **c** and **d**, the corresponding energy terms are shown, illustrating the heat rate for all the important processes (absorption, conduction, sublimation and radiation). In **a**, the signal is from the low fluence regime, and as can be observed in **c**, absorption and heat conduction are the significant processes. This will result in the peak LII temperature to be reached at the end of the laser pulse. The rapid signal increase during the heating is due to absorption being the dominant process, but as the laser pulse has passed, the heat loss by conduction will be dominant and cool the soot, hence the decreasing signal. For the high fluence case in **b**, peak LII temperature and signal will be reached during the laser pulse, just about the time when sublimation will be significant as shown in **d**. As sublimation will result in mass loss, the LII signal will start to rapidly decrease during the time of the laser pulse as shown in **b**.

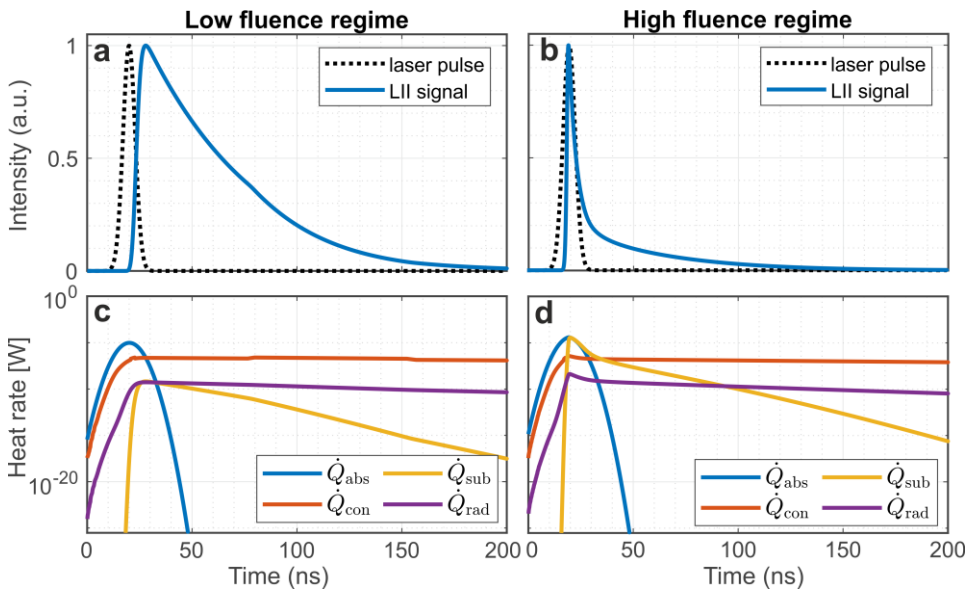


**Figure 3.8.** A comparison between the time resolved LII signal in relation to the heating pulse in the **a** low and **b** high fluence regime. In **c** and **d** the corresponding heat gain and loss rates are shown.

As observed in **Figure 3.8**, the LII signal appearance will depend on the laser fluence. An overview of the peak LII signal as a function of fluence for a certain type of soot is shown in **Figure 3.9**. The peak LII trend is shown as the red curve, namely the *fluence curve*.

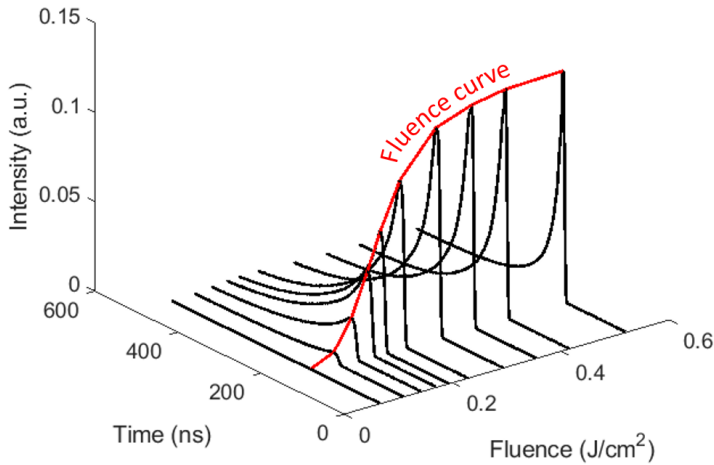


**Figure 3.9.** Time resolved LII signals are shown as a function of the laser fluence. The trend showing how the peak LII signal behaves as a function of laser fluence is termed the fluence curve.

The fluence curve shape, is strongly dependent on the LII setup, where different laser profiles will give decreasing, constant or increasing LII signal in the high fluence regime [68]. In the work presented in *Paper III* and *IV*, a top-hat profile was used to heat all investigated soot to the same extent.

### 3.2.2.8 Experimental considerations - Pulsed LII

LII measurements are most commonly performed using a pulsed laser configuration [48, 50]. The combination of pulse energy, wavelength and pulse length has to allow for the soot to reach high enough temperatures to incandesce as potential cooling by heat conduction can limit the peak temperatures. By the use of a Nd:YAG laser ( $t_{\text{pulse}} = \sim 5\text{-}10$  ns,  $\lambda = 1064, 532$  nm e.g., up to 1 J/pulse), a good combination of the mentioned properties will allow for measurements of LII on soot.

In *Paper III* and *IV*, results are presented from pulsed LII measurements aiming to study the absorption properties of soot, and to study the influence of rapid heating of soot of different maturity. In **Figure 3.10**, the double pulse system is showed, which essentially consists of the one pulse system, with an additional laser and an additional photomultiplier tube (PMT).

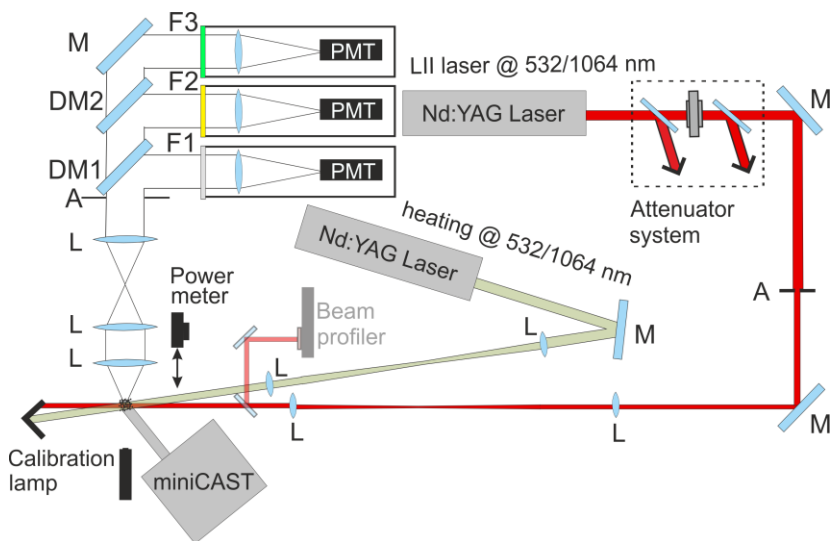


**Figure 3.10.** Experimental setup used for the work presented in Paper IV. The double pulse configuration with 3 PMTs are shown. For the work presented in Paper III, only one laser and two PMTs were used.

The lasers used are two Nd:YAG lasers (Quantel Brilliant B) operated at the fundamental wavelength of 1064 nm and the second harmonic wavelength of 532 nm. To maintain the spatial and temporal profile of the laser pulse, an external attenuation system is used to adjust the laser pulse energy, consisting of two thin film polarizers with a half-wave plate in-between. For the pre-heating laser, the Q-switch delay was used to adjust the pulse energy as the temporal profile was maintained in the used Q-switch delay range. For the two-pulse experiments, external triggering was performed for the lasers to maintain a given delay between the two pulses by the use of a digital pulse/delay generator.

On the detection side, achromatic doublets were used to collect the LII signal from the probe volume. Arranged as in **Figure 3.10**, the first lens collimates the light, while the second and third lens arrange the beam for the possibility of stray light reduction and to select the region of interest in the probe volume. Optical filters (and a mirror) are used to split the light into three wavelength ranges and three filters (Semrock 575/25, Semrock 684/24 and a 532 nm interference filter) are used to select the light of specific wavelengths for detection. Three photomultiplier tubes (2 Hamamatsu H10721-20 and 1 H6780-04) are then used for light detection [69]. The PMTs are connected to a 4-channel 1GHz digital oscilloscope (LeCroy Waverunner 104MXi) to allow for observation and storing.

A power meter (Ophire PE25BF-DIF-C) was used to measure the pulse energy of the laser. Performing qualitative measurements of soot absorption properties based

on fluence curve analysis requires accurate measurements of laser pulse energies in order to make reliable estimations of wavelength dependence and estimations of absorption efficiency. It is also of great importance to characterize the properties of the spatial beam profile for the purpose of accurate fluence estimations and for improved accuracy when performing LII modelling. For this purpose, a beam profiler was used (Gentec WinCamD).

### 3.2.2.9 *The LII model*

In the work presented in *Paper III* and *IV*, the LII model was used to reproduce experimental fluence curves in order to study the optical properties of differently matured soot, but also to study the influence of rapid laser heating on soot. For this purpose, the model was used to produce LII fluence curves for differently matured soot.

As the LII model is a tool based on heat and mass balance equations presented in Equation 3.11, where the most prominent physical processes (absorption, heat conduction, sublimation and radiation) are included. The equation is solved to produce time resolved LII signals. By varying different material parameters and experimental conditions, one may use the model to study the properties of the soot and its influence on the LII fluence curves. In the work presented in this thesis, the model developed by Bladh et al. was used [68], by considering the interaction of laser radiation with a single soot primary particle. As this is a much simplified view of soot, errors may be introduced as the important terms involved (absorption, heat conduction, sublimation) will be influenced by the aggregate shape (overlap of primary particles, shielding). It is however assumed that these parameters have a relatively small influence on the fluence curve as observations of collapsed and non-collapsed particles in [70] showed similar fluence curves despite morphology.

## 3.2.3 Elastic light scattering

### 3.2.3.1 *RDG theory for scattering by soot aggregates*

Rayleigh-Debye-Gans (RDG) theory is an approximation of the otherwise very complex description of scattering by an aggregate particle too large to be within the limits of the Rayleigh regime. RDG-theory assumes that each primary particle only interacts with the incoming electromagnetic field meaning that multiple scattering can be neglected. Also, the electromagnetic field is assumed to be static over individual primary particles [34, 41, 71].

Observing soot from a given angle  $\theta$ , the scattering intensity can be shown to scale strongly with the primary particle size  $d_{pp}^6$ , as the detected scattering light intensity  $I_s$  is given by

$$I_s = C_0 I_0 n N_a^2 k^4 \left( \frac{d_{pp}}{2} \right)^6 F(m) S(q) \quad (3.20)$$

where  $C_0$  is a constant with detection information,  $I_0$  is the incident light intensity,  $n$  is the aggregate number density and  $S(q)$  is the structure factor [33, 34]. The structure factor  $S(q)$ , describes the angular scattering function of a soot particle and is a function of the scattering wave vector  $q=2k\sin(\theta/2)$ , where  $\theta$  is the scattering angle and  $k$  is the wave vector  $k=2\pi/\lambda$ . The scattering wave vector  $q$  is an important quantity which carries information on the length scale of the scattering as it is the difference between the incoming and scattering vector [34].

For certain combinations of the product  $R_g q$ , the structure factor  $S(q)$  can be expressed as

$$S(q) = 1 \quad qR_g \ll 1 \quad (\text{Rayleigh regime}), \quad (3.21)$$

$$S(q) = 1 - \frac{1}{3} q^2 R_g^2 \quad qR_g \leq 1 \quad (\text{Guinier regime}), \quad (3.22)$$

$$S(q) = C (qR_g)^{-D_f} \quad qR_g > 1 \quad (\text{power law regime}), \quad (3.23)$$

in the Rayleigh, Guinier and power law regime, where  $C$  is a proportionality constant [34, 71] related to the pre-factor according to  $C=1.35/k_0$  [41].

As can be observed for the Guinier regime (Equation 3.22), measurements of scattering angle dependence can allow for estimation of  $R_g$ , regardless of the complex refractive index and other morphological properties. If the scattering behaviour is known in both Guinier and power-law regimes, both  $R_g$  and  $D_f$  could be estimated from Equation 3.22 and 3.23.

Further, from Equation 3.20 it can be observed that there is an inherent wavelength dependence as

$$I_s \propto \frac{1}{\lambda^4} F(m(\lambda)) S(q(\lambda)) \quad (3.24)$$

where the wavelength dependence of the scattering intensity will depend on the scattering function and by that on the complex refractive index. It may hence be of

interest to both investigate the scattering angle dependence and the scattering wavelength dependence, retrieving both information on the morphology and on the bulk optical properties.

### 3.2.3.2 The nephelometer

In **Figure 3.11**, an illustration shows the nephelometer (Aurora 3000, Ecotech [72]) presented in *Paper II* from side view, showing the position of the light source, detector and measurement volume for **a** integrated total scatter mode with the scattering angles of 9-170° and, **b** integrated backscatter mode with the scattering angles of 90-170°. The light source consists of a 3x3 array of light emitting diodes of the wavelengths of 450 nm, 525 nm and 635 nm. Hence, the provided information from the nephelometer is the wavelength- and integrated angle-dependent scattering cross-section  $\sigma_p$  (p for particle) of the aerosol particles passing through the optical chamber.  $\sigma_p$  can be measured as calibration using particle-free air and CO<sub>2</sub> is performed, allowing for the scattering due to the carrier gas to be subtracted and the absolute value of  $\sigma_p$  to be obtained.

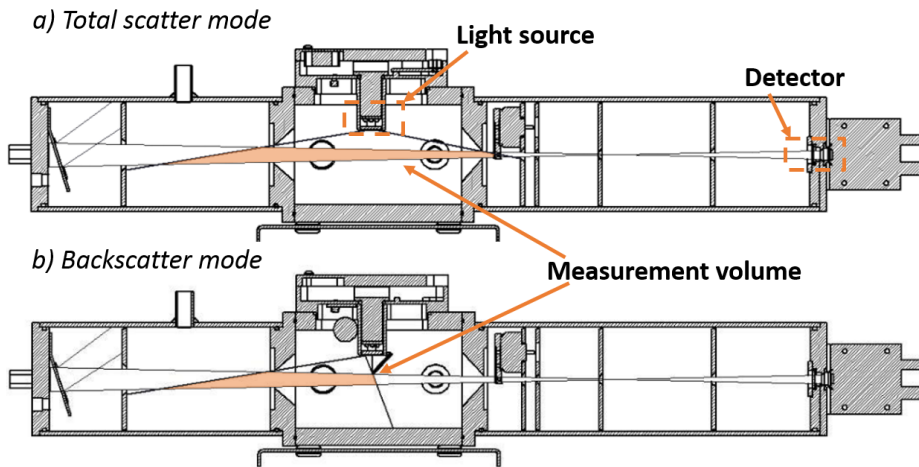


**Figure 3.11.** An illustration of the Aurora 3000 nephelometer (Ecotech), showing a) full scatter mode and b) the backscatter mode. The marked orange area shows the measurement volume for the two cases. The position of the light source and the detector is shown. The figure is based on the illustration in [72].

In *Paper II*, an expression of the scattering Ångström exponent (SAE) was derived from the geometry of the nephelometer measurement volume and RDG-theory as shown below,



$$SAE = -\frac{\ln(G(\lambda_1)/G(\lambda_2))}{\ln(\lambda_1/\lambda_2)} - \frac{\ln(F(\lambda_1)/F(\lambda_2))}{\ln(\lambda_1/\lambda_2)} + 4, \quad (3.25)$$

where  $G(\lambda)$  describes the integrated scattering intensity at a given wavelength detected by the nephelometer. The first term on the right hand side only depends on the morphology of the soot, while the second one only depends on the refractive index of the soot. This will allow for the determination of the  $F(m,\lambda)$ -ratio if the morphology and the wavelength dependence of the soot is known.

### 3.2.3.3 Elastic light scattering

In *Paper IV*, the scattering by soot aggregates is observed during LII measurements when using the wavelength of 532 nm. In the low fluence regime it is expected that the soot will not be influenced by sublimation and hence the peak ELS signal should appear at peak laser energy, nevertheless, the soot scattering properties may be influenced by the change of the soot temperature, which is the highest at the end of the laser pulse. As the time of peak T will vary depending on the input energy, it will also dictate the time of sublimation. Hence, peak ELS during LII measurements will be influenced by the time of peak T and cannot be directly used to obtain any information about the size of the aggregate by assuming a scattering intensity proportional to  $d^6$  as given by Equation 3.20. Hence, in *Paper IV*, a methodology is adapted from analysis using single particle soot photometer (SP2) termed leading edge fit [73]. The leading edge fit essentially fits the temporal laser profile to the scattering signal, suggesting the actual scattering signal as if no mass would be lost during particle heating. The principle is showed in **Figure 3.12**.

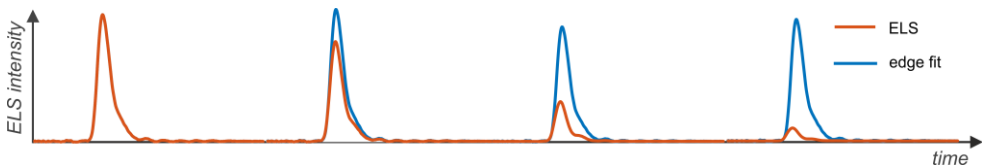


**Figure 3.12.** Four ELS signals are shown of different signal intensity and shape. A signal which represents the laser temporal profile is fitted to the leading edge of the ELS signal, simulating how the signal would appear if no mass loss would occur. The fitted signals are normalized.

## 3.3 Aerosol diagnostics

The work presented in this thesis is mainly based on the use of optical diagnostics, nevertheless some introduction will be given to the aerosol diagnostic techniques used in the work of *Paper I* to improve the understanding of the results.

### 3.3.1.1 *Aethalometer*

The aethalometer is an instrument which operates filter-based optical measurements. The instrument used in the work of *Paper I* is a AE33 from Magee Scientific and operates with 7 wavelengths (370, 470, 520, 590, 660, 880, 950 nm) with the dual spot technique [74]. As aerosol particles are deposited on a filter, the attenuation will be measured through the filter at the given 7 wavelengths. The principle is straightforward, however filter effects complicate the procedure. As the attenuation is derived at multiple wavelength between 370 and 950 nm, the wavelength dependence of the absorption can be measured. By assuming that all absorption at the longest wavelength is absorbed by refractory soot,  $MAC_{\text{aethalometer}}$  may be used to obtain the equivalent BC (eBC) mass. The instrument operates best at concentrations below  $150 \text{ ng/m}^3$ .

### 3.3.1.2 *Scanning mobility particle sizer (SMPS)*

The SMPS consists of a bi-polar charger, differential mobility analyser (DMA) and a condensation particle counter (CPC) and measures the mobility diameter of aerosols. The DMA is the instrument which allows for determining the mobility diameter of soot aggregates, while the CPC counts the number of particles. The mobility diameter of a regular soot aggregate scales roughly with the radius of gyration, but depends on the number of primary particles in the soot [75].

### 3.3.1.3 *Soot particle aerosol mass spectrometer (SP-AMS)*

The soot particle aerosol mass spectrometer (SP-AMS) allows for analysis of refractory soot. In the work of *Paper I*, the Aerodyne SP-AMS was used in dual-vaporization and standard AMS mode, which allows for mass spectrometry of aerosol which may fragment upon hitting a tungsten plate of  $600 \text{ }^\circ\text{C}$ , or when also passing a Nd:YAG intra-cavity laser which will vaporize the refractory soot too [76]. Hence, the fragments from vaporization may be used to identify parent molecules of the soot, and to obtain information about the properties of the refractory soot [77].

### 3.3.1.4 *Thermo-optical analysis*

Thermo-optical analysis, or as it is often referred to '*OC/EC analysis*', provides a measure of the components of a carbonaceous aerosol particle. By observing how the particle will evaporate, pyrolyse and oxidize in an inert or weakly oxidizing atmosphere while ramping the temperature, the total carbon (TC) particle composition can be divided into organic carbon (OC), pyrolytic carbon (PC) and elemental carbon (EC), where OC is the non-refractory component, PC is OC which is charred during the heating in an inert atmosphere, and EC is the refractory component of soot. PC can falsely be interpreted as EC, and it is hence generally considered a source of error. The protocol used in *Paper I* is the EUSAAR\_2 shown

in **Figure 3.13**. During the temperature ramping in the initial He-atmosphere non-refractory organic carbon components can evaporate depending on their volatility. As oxygen is then introduced, the elemental carbon component of the soot will start to oxidize at the elevated temperature. To trace how much material has been volatilized at each measurement step, the emitted volatiles are oxidized to CO<sub>2</sub> and further converted to methane which is then detected in a flame ionization detector (FID), which is shown along with the protocol in **Figure 3.13** as the blue coloured graph. To correct for the charring during measurements, a laser detection system measures the attenuation at 633 nm through the filter to account for increasing absorption due to the charring in the initial He environment [78]. The instrument used for the thermo-optical analysis in *Paper I* is a DRI carbon analyzer model 2001

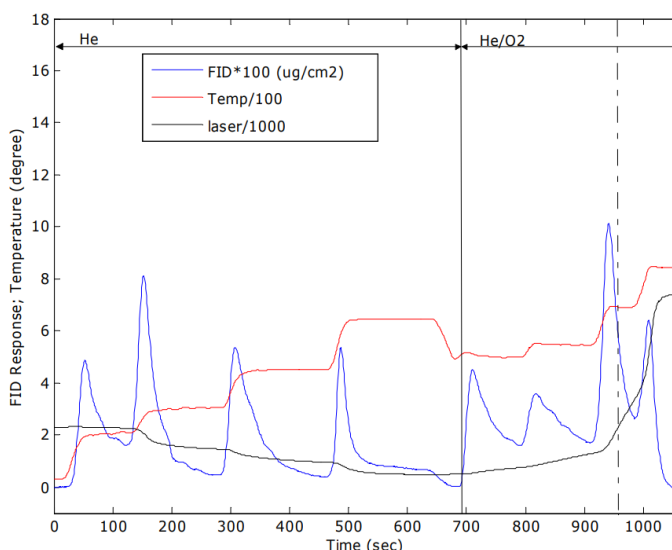


**Figure 3.13.** The EUSAAR\_2 protocol follows the temperature ramping according to the scheme shown with the red line. The first ~700 s are in an inert He atmosphere while the final ramping is done in the oxidizing atmosphere with 2% O<sub>2</sub>. The figure is adapted from [78].

# 4 Results

The work presented in this thesis related to the diagnostics of soot from a mini-CAST is described in detail in *Paper I-IV*. In this section, the highlights of these papers will be summarized and discussed in relation to the aims and objectives presented in Section 1.3. In addition, some supplementary results are presented to facilitate the understanding of the results.

## 4.1 Characterization of soot of various maturity and morphology

### 4.1.1 Optical and physicochemical properties

The optical properties of differently matured soot depends on 1) the bulk soot material properties and 2) the morphology of the soot. Hence, to grasp how different types of soot may interact with solar radiation, it is of importance to study material and shape parameters in relation to optical properties. Hence it was investigated how the optical properties of the different types of mini-CAST soot was related to the physicochemical properties of the soot. Specifically it was investigated how the BrC properties of the young soot was related to the non-refractory and refractory components of the soot. As pointed out in the work by Saleh et al. [13], the brown-black continuum may describe the whole spectrum of carbonaceous particles such as soot [13], where in *Paper I* it was observed that young ‘immature’ mini-CAST soot may have BrC-type of absorption properties while mature mini-CAST soot is BC-like.

A multi-wavelength (multi- $\lambda$ ) extinction setup was used to measure the absorption at 4 wavelengths (405 nm, 650 nm, 850 nm and 1064 nm) to determine the absorption Ångström exponent (also known as the dispersion coefficient  $\xi$ ; see Section 3.1.1), which describes the absorption wavelength dependence and is usually  $\sim 1$  for mature soot and  $>1$  for young soot. For comparison and validation, an aethalometer was used to obtain the *AAE*, although the aethalometer measures the attenuation through soot deposited on a filter (see Section 3.3). An SMPS was used to monitor the size distribution of the polydisperse soot, an SP-AMS was used

to study the composition of the soot, and samples of soot were collected for thermo-optical analysis for information on the OC/EC ratio of the soot, and for TEM analysis (however presented in Malmborg et al. [77]). The full setup can be seen in detail in Figure 1 in *Paper I*.

In order to investigate how refractory and non-refractory components of the soot contributes to the absorption, a thermodenuder and an oven was used to heat the particles to 250 °C and 500 °C respectively, to remove volatile material. In **Figure 4.1**, the AAE is shown for all the studied mini-CAST soot, with and without heat treatment. It can be observed that for the multi- $\lambda$  extinction measurements, the AAE increases for soot with higher OP number. The AAE for OP1 and OP3 soot are  $\sim 1.3$  while for OP5-7 soot it is in the range 1.5-3.5. The stronger wavelength dependence, i.e. higher AAE, indicates that species absorbing at the shorter wavelengths may be present or there may be an overall stronger wavelength dependence of the refractory soot. As the soot is heat treated by passing through the thermodenuder or the oven prior to detection, the AAE will decrease for OP5-7 but stay unchanged for OP1 and OP3. The decreasing AAE with pre-heating for OP5-7 indicates that evaporating species might responsible for some absorption at least at the shorter wavelengths, inducing a change in the overall AAE. I may however be speculated whether the rest of the soot remains as unaltered.

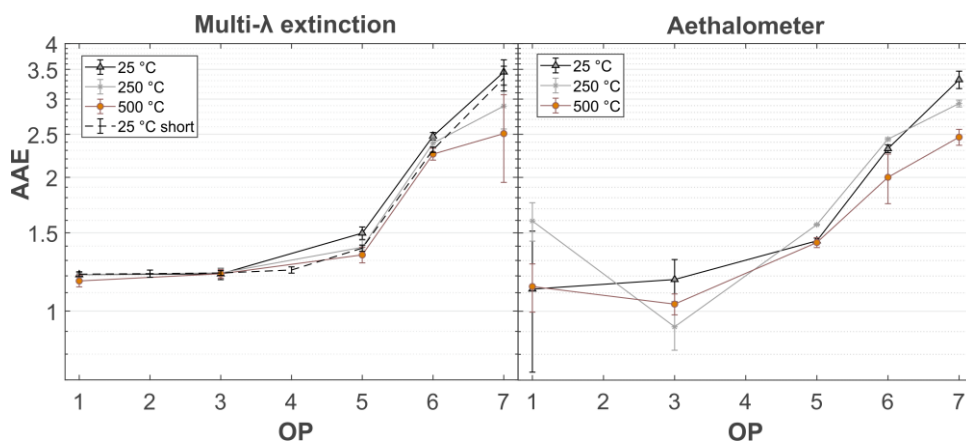


**Figure 4.1.** The AAE for the mini-CAST soot (OP1, OP3 and OP5-7) from the multi-wavelength and aethalometer measurements. There is a clear trend showing the dependency on operation point (OP) and for the extinction measurements there is a significant trend as a result of heating in a thermodenuder (250°) and oven (500°) prior to measurements. Note that the y-axis is logarithmic.

But to investigate whether the assumption of negligible scattering is valid for the set of measurements, the influence of soot coagulation on the AAE was considered. The setup used in *Paper I* involved transportation in pipes between the set of instruments which resulted in residence times which may cause soot coagulation throughout the

piping. Hence, the multi-wavelength extinction measurements were repeated on fresh mini-CAST soot closer to the soot source (with 1/5 of the residence time of the main measurements), allowing estimation of *AAE* prior to extensive coagulation. The resulting geometric mean diameter (GMD) for the different cases are shown in **Figure 4.2** where large difference in GMD can be observed for the main measurements and the repeated measurements. Considering the *AAE* for the repeated measurements, results show no influence of coagulation on *AAE* for the large soot (OP1 and OP3) despite the large difference in mode size, for the smaller soot (OP5-7) there appears to be a small difference but it is considered negligible in the context. Hence, the influence of scattering on the estimations of *AAE* can be considered negligible.

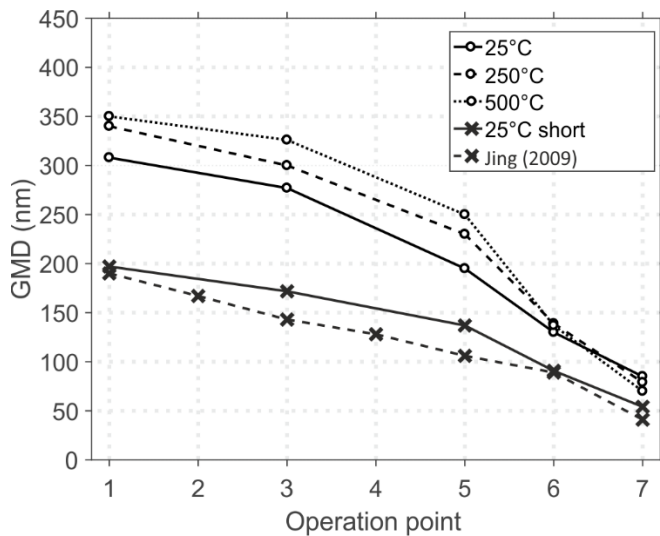


**Figure 4.2.** The geometric mean diameter (GMD) of the soot depending on the experimental configuration. For the main measurement series (25 °C, 250 °C, 500 °C), the residence times were long compared to the repeated measurement (25 °C short) which shows the large differences in size due to coagulation. The increasing GMD with heat treatment for OP1, OP3 and OP5 soot is related to the residence time  $t_{res}$  of the soot where  $t_{res} = 17$  s, 31 s, 45 s respectively for the BP, TD and Oven measurements while the decreasing GMD with heating of OP6 and OP7 soot is related to the extent of mass loss.

Thermo-optical analysis (Section 3.3) was performed on the samples collected from each measurement case to obtain information on soot composition divided into EC, OC and PC (and TC; see Section 3.3). The results of the OC fraction (OC/TC) and OC+PC fraction ((OC+PC)/TC) are shown in **Figure 4.3**. Both OC/TC and (OC+PC)/TC are shown for all cases and it can be observed that for the OP1, OP3 and OP5 soot, the soot is dominated by EC. For OP6 and OP7 however, the concentrations of OC and PC are significantly higher and will decrease due to heat

treatment. For OP7, where the particle concentrations are the lowest and hence it has the most optimal circumstances for aerosol measurements, it can be seen that the fraction of OC and OC+PC decreases when heated prior to investigation. As it is known that the interpretation of the thermo-optical results of BrC soot can be quite complex as it appears that the soot will be altered during the thermo-optical evaluation procedure [79, 80], care has to be taken when analyzing the results. For example in [79], mini-CAST soot was investigated while exposed to the heating scheme of a thermo-optical analysis (however using a different protocol generating more PC; NIOSH870). It was observed that for BrC type of mini-CAST soot, there was a large structural change of the soot at the highest temperature step (870 °C) in the He environment, and also it was seen that the BrC soot had the same properties as the BC soot at the final heating steps.

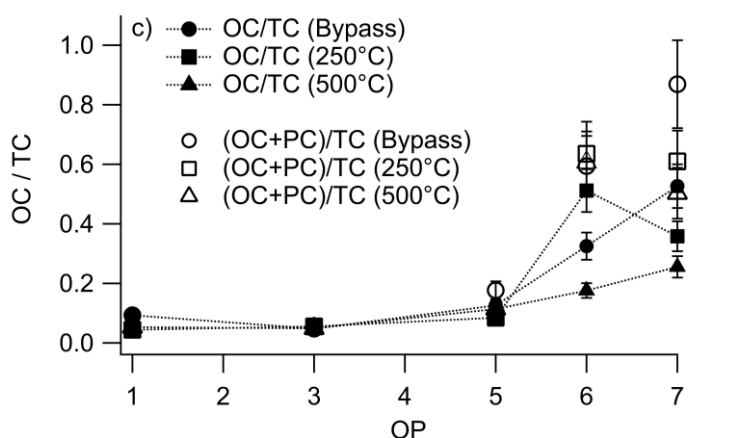


**Figure 4.3.** The thermo-optical analysis of the mini-CAST soot with and without pre-heating. OP1, OP3 and OP5 mainly consist of EC, while OP6 and OP7 consists of a substantial amount of OC and PC.

In **Figure 4.4**, an overview is given of the OP1 and OP7 soot composition, normalized to the EC content of the soot (or assuming that the EC content of the soot is constant and independent of heating). The figure shows how the composition for these two types of OP soot changes from the reference case at room temperature (bypass (BP)), to heating at 250 °C (thermodenuder (TD)), and finally to heating at 500 °C (Oven). For OP1 there is as previously observed only a minor contribution of OC, but for OP7 there is a substantial difference. More than half of the OC+PC content is removed when heated to 500 °C and it can be observed that both the OC and PC fraction decreases but is not removed entirely. It is especially interesting that the part of the soot which experiences charring during the heating scheme will not be removed at a special temperature step, but appears to be present after both by-pass, thermodenuder and oven heating. Since the soot material is altered during

the procedure of the thermo-optical analysis, the components OC, PC and EC are specifically related to the heating scheme, as both temperature and time are important parameters in the investigation and will influence the final results.

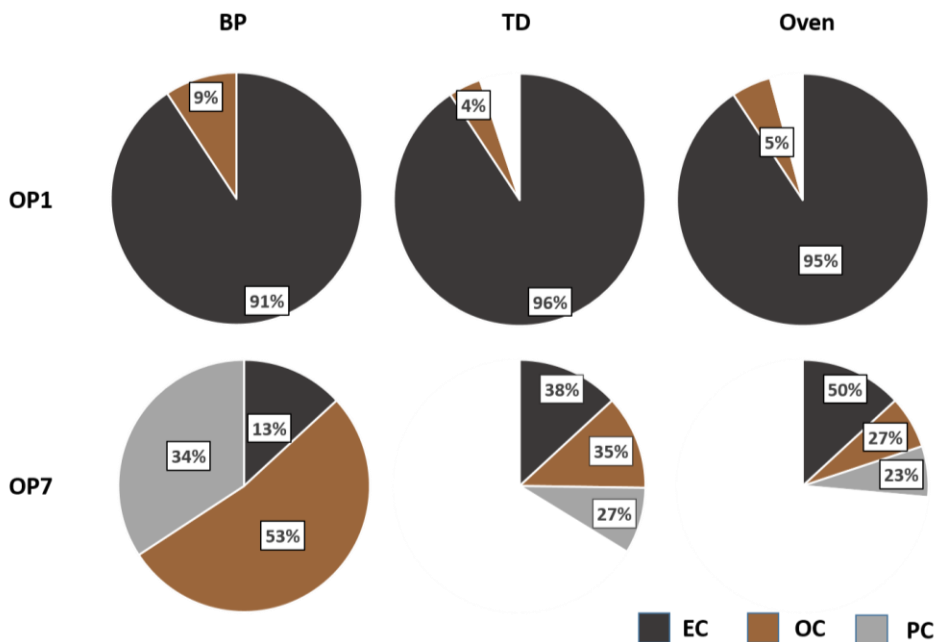


**Figure 4.4.** The composition of OP1 and OP7 soot before and after different stages of pre-heating. The concentrations are normalized to the EC content, assuming the mass to be independent of heating. For OP1 only a small change is observed, as some OC is evaporated when pre-heated. For OP7 however, a large fraction of the OC and PC is removed in the thermodenuder (TD) and even more in the Oven.

From SP-AMS measurements it was showed that the organic aerosol (OA), which represents the fraction of the soot which evaporates upon hitting a tungsten vaporizer at 600 °C, was mainly shown in the work presented in *Paper I* to consist of aliphatics and PAHs. As further discussed in *Paper I*, the OA mass appeared to correspond to OC1 and OC2 masses from the thermo-optical analysis, failing to detect the less volatile OC and PC of the soot [77] (*Paper C*) which highlights the difficulties of comparing technique specific evaluation of a particular sample. It was discussed in *Paper I* that the OC3, OC4 and PC of the younger soot may be incorporated in the refractory carbon matrix from the SP-AMS results. It was further discussed in [77] (*Paper C*) that the less volatile OC might not be able to evaporate on the timescales used in the AMS mode. It could however potentially pyrolyze as during thermo-optical analysis in He environment, and hence be included in the refractory BC during SP-AMS mode.



Two refractory soot mass spectra from SP-AMS measurements are shown in **Figure 4.5**, i.e. mass spectra from the soot core only. The mass spectra of OP1 and OP7 soot are shown of the fragments generated upon laser vaporization, dictated by the bonding structure of the soot bulk material. It can be seen that the mature OP1 soot generated smaller carbon fragments ( $C_1^+ - C_5^+$ ), while the younger OP7 soot favoured the formation of relatively larger carbon fragments ( $>C_5^+$ ). Heat treatment of the soot prior to the SP-AMS measurements gave no significant change of the mass spectra from the refractory soot core. This may indicate that there is no influence on the refractory soot core from the heating from neither the thermodenuder nor the oven.

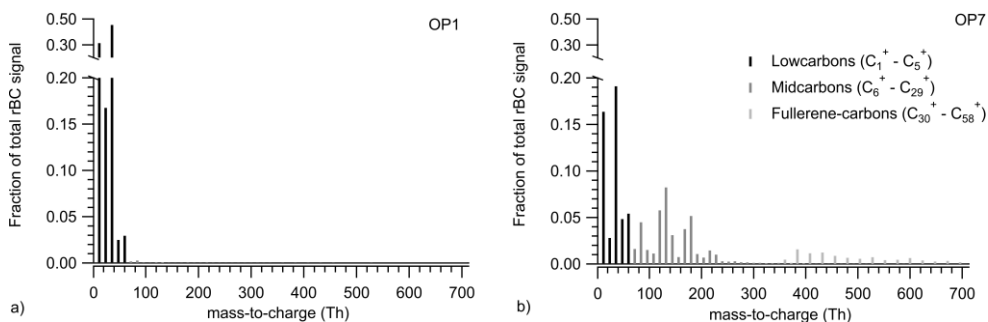


**Figure 4.5.** The soot mass spectra of OP1 and OP7 soot from the SP-AMS using laser vaporization to evaluate the refractory soot. Depending on the maturity of soot, different types of soot fragments will be generated during laser vaporization, related to the soot bonding structure.

Further in *Paper I*, the absorption properties related to the OC+PC and EC was investigated, assuming that only EC absorbs at the highest measurement wavelength, while it was expected that the  $MAC_{OC+PC}$  should be lower than  $MAC_{EC}$ . It was shown that for  $MAC_{EC}$  to be higher than  $MAC_{OC}$ ,  $AAE$  for EC would have to be higher than 1 for the young soot types. This suggests that the soot with a high  $AAE$  cannot be described by a core-shell model with a mature refractory BC core and an organic coating, but rather suggesting that the OP6 and OP7 soot is BrC like soot of low maturity.

The use of different measurement techniques can categorize soot into different components, such as e.g. OA, OC, PC, EC, rBC and eBC, hence it may be intuitive to consider soot as composed of different types of materials. However, one must keep in mind that these components are defined in relation to specific measurement techniques. As there is no general categorization, and the evaluation related to each measurement technique is complex, evaluation and comparison has to be made with caution.

### 4.1.2 Investigations of soot morphology

As observed during the measurements presented in *Paper I*, not only did the absorption properties vary with the soot from the different mini-CAST operation points, but also the sizes varied as given by **Figure 4.6**. The figure shows that there is a distribution of particle sizes at each height and that the soot particle diameter (the mobility diameter  $d_m$ ) in general is larger for lower OP soot case. This is expected as the highest OP number soot, OP7, consists of soot quenched early in the soot formation process of the sooting flame, and the lowest OP number soot, OP1, is quenched at a flame position where soot formation has occurred during much longer time (see **Figure 2.5**). The size and morphology of soot from real-life combustion sources influence how they will interact with solar radiation and hence influence their radiative properties [34, 41].

As presented in Section 3.2.3, there is a strong connection between the scattering angle dependence of soot aggregates (structure factor), and its morphological properties. Given by Equations 3.21-3.23, the different scattering regimes depending on the angle and the size of the aggregates are shown, where different relationships between scattering angle dependence and morphology are given. The usefulness of investigating the scattering wavelength dependence to solve an inverse scattering problem is especially considered in the Guinier regime, where it is well posted for determining  $R_g$ . This has been utilized by many researchers and is much explored in the field [34, 81-86].

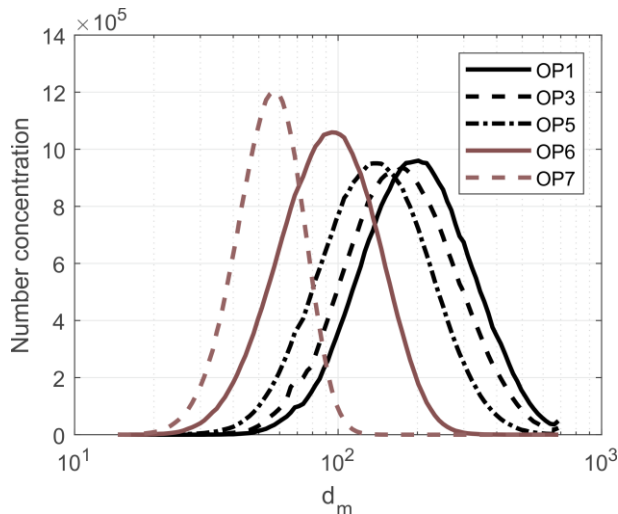


**Figure 4.6.** The log-normal size distribution of the different types of mini-CAST soot using a SMPS system. The diameter shown is the mobility diameter  $d_m$ . It is clearly shown that the mode size decreases with increasing OP number, with mode diameters ranging from 200 nm down to 60 nm.

In the work of *Paper II*, an integrating nephelometer (Aurora 3000, Ecotech) was used for scattering measurements on the soot as part of an investigation of the feasibility of using the nephelometer in combination with RDG-theory to estimate morphological parameters of soot. As described in Section 3.2.3, the nephelometer provides the integrated forward to backward scattering ratio  $Q$  (FW/BW) providing information about the shape of the particle as it largely dictates the structure factor  $S(q)$  of the soot e.g. with a larger  $Q$ , the larger the particle. As the measurements are done at three wavelengths, the wavelength dependence of the scattering (scattering Ångström exponent,  $SAE$ ) will also be provided by the nephelometer. Obtaining  $SAE$  may allow for determination of the scattering function wavelength dependence ( $F(m, \lambda_1) / F(m, \lambda_2)$ ) and hence a wavelength dependence of the complex refractive index in the given wavelength range ( $\lambda_1 - \lambda_2$ ).

The nephelometer results are shown for OP1-8 soot in **Figure 4.7**, where clear trends can be observed. The low number OP soot, such as OP1-3, are of mature character and of larger sizes, while the higher the OP number is, the less mature is the soot produced and the soot aggregates become smaller and even individual primary particles. It can be observed to the left side of the figure that  $Q$  is higher for low OP-number soot, while the  $SAE$  is lower. On the right hand side for high-number OP soot,  $Q$  is approximately 1 and  $SAE$  is approximately 4, which is valid for scatterers in the Rayleigh regime.

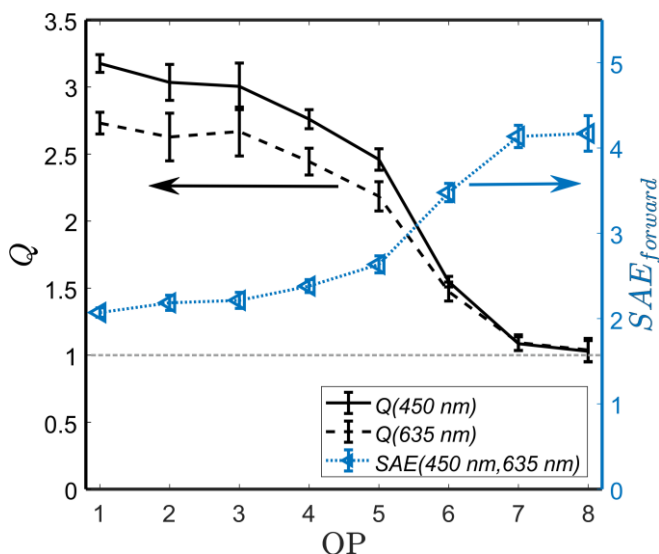


**Figure 4.7.** The forward-to-backward scattering ratio is shown as the black lines following the left y-axis, while the  $SAE$  is the blue curve following the right y-axis. As the different soot types are of decreasing size with increasing OP, the results show the trend as a function of aggregate size.

As discussed in Section 3.2.3, it can be expected from very small soot particles with a wavelength-independent complex refractive index, that the scattering will follow a  $1/\lambda^4$  relationship ( $SAE=4$ ) and that the scattering will be equally much in the forward and backward direction i.e.  $Q=FW/BW=1$ , as small particles will fulfil the criterion for the Rayleigh regime. But as the aggregate grow larger in size, the  $SAE$  will deviate from 4 and  $Q$  will increase. In addition, the spectral dependence of the complex refractive index will also influence  $SAE$  as shown by the second term on the right hand side of Equation 3.25.

As shown by the RDG-theory applied on numerically generated soot aggregates presented in *Paper II*, the nephelometer may be used to obtain information about the morphology in terms of the radius of gyration  $R_g$  and the fractal dimension  $D_f$  for aggregates of  $R_g < 185$  nm. The limit of  $R_g < 185$  nm is based on the fact that for these particles the inverse problem is well-posed as they are considered small enough to remain outside of the pure power-law regime where determination of  $R_g$  and  $D_f$  is not possible anymore.

By comparing the scattering properties of numerically generated aggregates with the mini-CAST soot, estimations of  $R_g$  and  $D_f$  was obtained (shown in Table 1 in *Paper II*). As can be observed, the estimations of  $R_g$  deviated some from the TEM results. Different reasons for the discrepancy can be found, such as the polydispersity of the mini-CAST soot, suggesting that the  $R_g$  may be overestimated as larger aggregates scatter more efficiently. The accuracy of the RDG theory can also be a factor that influences the accuracy of the results, as it may induce an error of  $\sim 7\%$  on the  $Q$  as discussed in *Paper II*. Further, when making this comparison another difference should be considered and this is an uncertainty in the degree of coagulation of the soot. For the TEM analysis soot was sampled just after mini-CAST soot generator, whereas the nephelometer measurements were made on soot that had longer residence time that could result in some coagulation.

Further it was observed that from the relationship in Equation 3.25 the wavelength dependence of the scattering function  $F(m, \lambda)$  may be estimated, indicating a wavelength dependence of  $m$ , which is related to the dispersion coefficient of soot. In agreement with the estimations by Bescond et al. [40], the  $F(m, \lambda)$ -ratio decreases with soot maturity in the wavelength range investigated.

A nephelometer such as the Aurora 3000 can hence be a good candidate to perform estimations of morphological parameters of soot aggregates in aerosol phase, and as a good alternative to TEM analysis. Also as the  $SAE$  depends on both the morphology and the wavelength dependence of the scattering function, information about the scattering function wavelength dependence can be obtained, which has been shown to be related to the maturity of soot. Hence the nephelometer may also be used to give indications about the bulk properties of the soot.

## 4.2 Soot-laser interaction

In *Paper III* and *Paper IV*, work is presented where LII is used to study the absorption properties of soot and investigate the response of young soot to rapid laser heating.

### 4.2.1 1-pulse experiments

As discussed in Section 3.2.2, LII can be considered an indirect absorption technique, as there is no influence of scattering on the LII signal, which is detected at a wavelength different than the laser excitation wavelength. Hence, in the study presented in *Paper III*, LII was used to study the absorption properties of the mini-CAST soot to investigate potential differences in relation to the results from the extinction measurements presented in *Paper I*.

LII is as described and discussed in Section 3.2.2 a technique which relies on the rapid heating of soot using a short laser pulse, heating it to incandescing temperatures of 2000-4000 K. In *Paper III*, fluence curves for 3 types of differently mature mini-CAST soot (OP1, OP6 and OP7) were investigated in order to obtain information on the absorption efficiency, to investigate the use of LII to obtain the dispersion coefficient, and to estimate the absorption function for the soot by analysis of the fluence curve in the low fluence regime.

In **Figure 4.8** the fluence curves are shown for the two excitation wavelengths and the two detection wavelengths in the study. In **a**, the fluence curves are shifted along the fluence axis, showing that much less energy is needed to heat the OP1 soot to its maximum LII signal, than for the young soot (OP6 and OP7 soot). Hence, information about the absorption efficiency can almost directly be observed, however many other parameters than the absorption efficiency may influence the behaviour of the fluence curve (e.g. physicochemical and morphological properties). Further it can be expected that conducting LII on young soot will result in interference from fluorescing species when an excitation wavelength below  $\sim 700$  nm [87] is used, see **b** where this can be observed as the fluence curves overlap and as the detection wavelength has a strong influence on the curves. The interference can be circumvented by considering the LII signal at the time beyond the lifetime of the laser-induced fluorescence [88, 89]. By considering the LII signal at 50 ns after the peak LII, a delayed LII curve can be obtained allowing estimation of the absorption wavelength dependence expressed as the dispersion coefficient  $\xi$  (Section 3.1.1).

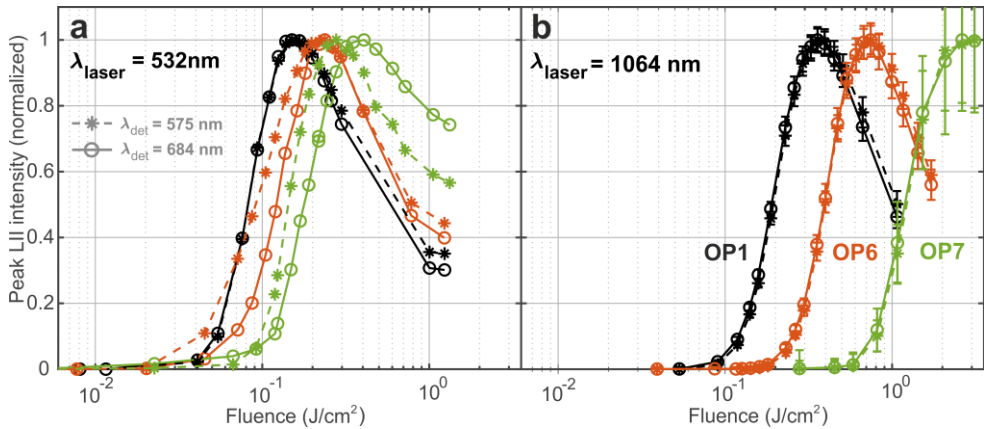


**Figure 4.8.** In a, the fluence curves are shown for OP1, OP6 and OP7 type of soot using an excitation wavelength of 532 nm for the two detection wavelengths at 575 and 684 nm. In b, the same is plotted but when a laser excitation wavelength of 1064 nm is used. It is suggested that LIF may be influencing the signal for the case of 532 nm excitation wavelength, as the prompt LII signal (averaged over 4 ns) is considered.

In **Figure 4.9**, examples of temporal LII signals are presented for the three types of mini-CAST soot (OP1, OP6, OP7), normalized to the peak point. As can be observed, the decay time varies quite extensively, most likely related to the differences in heat conduction due to differences in primary particle sizes, and possibly also due to differences in thermal properties. As the less mature soot (OP7) gives rise to a very short temporal LII signal, difficulties will arise when considering the LII signal at a delayed time after peak LII, see **Figure 4.9** where a temporal LII signal is shown for OP1, OP6, and OP7 soot. The short temporal LII signal may cause suspicion as it is of approximately the same lifetime as LIF, but as the signal is observed using a laser wavelength of 1064 nm, this potential interference can be ruled out and hence can be treated as the OP1 and OP6 soot in the evaluation procedure.

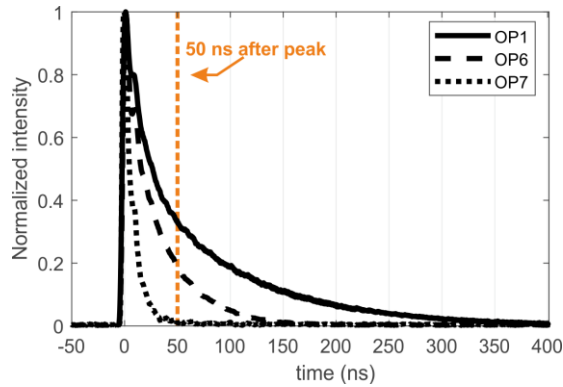


**Figure 4.9.** The time resolved LII signals are shown for peak LII for the three different soot types. The decay rate is more rapid for the smaller and less mature case, where heat conduction appears more efficient due to the larger surface to volume ratio.

The resulting dispersion coefficients are shown in **Figure 4.10** together with the extinction-derived ones, and as can be observed results show good agreement for the mature soot, while the young soot appears to have a lower  $\zeta$  when estimated with LII. The discrepancy between the two techniques may have to do with 1) the influence of rapid heating of the young soot, 2) with the wavelength ranges used for the two techniques, and 3) with the experimental procedure in *Paper I*. The potential influence of volatiles which require energy to evaporate when heated may also influence the evaluated  $\zeta$ , but would result in an even bigger discrepancy as volatiles are expected to absorb more efficiently at 532 nm.

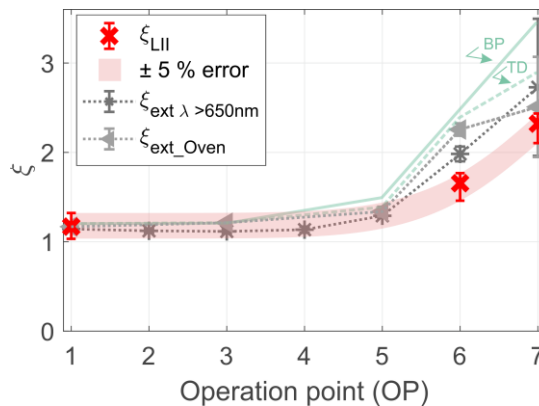


**Figure 4.10.** The experimental  $\zeta$  from the fluence curve analysis is shown for OP1, OP6 and OP7 soot. The results are compared with estimated values using multi- $\lambda$  extinction in *Paper I*, where the gray curves show the results if wavelengths above 650 nm are used or when the soot has been heated in an oven at 500 °C. The green curves show the results from non-heated and soot heated in a thermodenuder at 250 °C using all wavelengths between 405-1064 nm.

The soot absorption efficiency can as previously discussed in Section 3.1.1 be expressed as the absorption function  $E(m,\lambda)$ , which is a common and important parameter considered in the LII community. In Section 3.2.2 it was further discussed that the fluence curve analysis may allow for estimation of the  $E(m,\lambda)$  by analyzing the fluence curves at the low fluence regime. Here the temperature of the soot is high enough to have a relatively constant volumetric heat capacity but still sublimation is negligible. By investigating the evolution of the soot temperature, the absorption function can be estimated using Equation 3.16, derived in Section 3.2.2. In **Figure 4.11a** the temperature evolution is shown, where the region of interest is indicated. It can be observed that the temperature increase appears linear in the regime of interest. From the estimations, an  $E(m,\lambda)$  for OP1 soot was found to be 0.33, which agrees well with the estimations of [40], a value which appears reasonable as it agrees well with estimations of mature soot in the literature, where it is reported to fall in the range of 0.32-0.40 for mature soot at 550 nm [37].

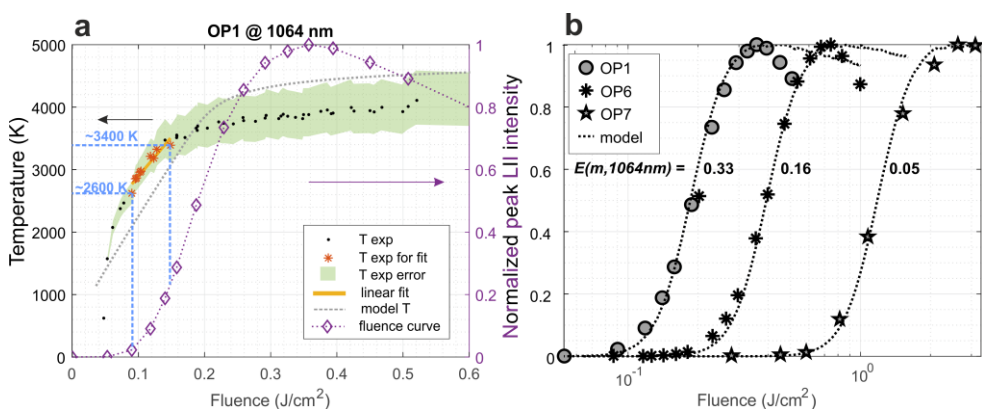


**Figure 4.11.** In **a** the fluence curve of OP1 soot is shown along with the peak LII temperature evolution. In the low fluence regime, the temperature data is investigated in a region of sufficiently good signal and below 3400 K (red stars), above which sublimation is expected to be significant [54]. The LII temperature regime of interest is marked with the blue dashed lines and is shown to range between ~2600-3400 K. The fit to the data is shown as a yellow line. In **b**, the experimental fluence curves are shown together with modelled fluence curves. The estimation of  $E(m,\lambda)$  for the different OP soot is also included in the figure.

For the OP6 and OP7 soot, the LII model was used to estimate the  $E(m,\lambda)$  based on the relation to the OP1 fluence curve. In **b** the modelled fluence curves are shown along with the experimental curves and the resulting  $E(m,\lambda)$ . It should however be kept in mind that not just the absorption properties of the soot types are different. Also the aggregate size, primary particle size, and amount of volatiles differ. It was shown using simulations with the LII model that the parameters related to the thermal and shape properties of soot had a minor influence on the fluence curves, and thereby the evaluated  $E(m)$ . Other sources of error may be differences in



sublimation temperature [54], differences in sublimation properties (e.g. what type of fragments are generated), and the potential influence of volatile species co-emitted with the refractory soot. Even if considering the influence of a non-absorbing coating (with the thermal properties of oleic acid [90]) on the soot as discussed in *Paper III* supplemental information, the estimated absorption properties would still be at approximately 0.065 for OP7 soot with an evaporating part constituting 86 % of the soot.

The LIF contribution from organic compounds to the LII signal was excluded from the analysis when investigating the absorption properties of the soot, but it may also be isolated to obtain the LIF contribution during measurements. It was shown that for OP1 soot, there was no LIF contribution, but as expected, substantial LIF signal was observed for OP6 and OP7. As the wavelength of 532 nm was used to induce the fluorescence, large PAHs (more than 5 rings) will be responsible for the signal [87, 91], and possibly from the young refractory soot itself.

#### 4.2.2 2-pulse experiments

LII which is a common laser-based technique used for soot diagnostics is usually considered non-intrusive as optical *in-situ* techniques usually are. Nevertheless it is well known that rapid laser heating of soot will actually alter the internal bonding structure by thermal annealing, if the soot reaches high enough temperatures for a sufficiently long time [56, 64-66, 92-95]. As shown early by Vander Wal et al. [65, 66], laser heating of soot changes the nanostructure by increasing the order of the graphitic structure of the soot. If enough energy and time is given, an onion-ring type of shell structure with graphitic carbon layers aligned with the surface of the soot will be induced. It was also shown in [66] that higher LII signals were obtained after soot had been pre-heated with an earlier pulse, which was related to the thermal annealing of the soot material, changing its absorption and emission properties. Since the work by Vander Wal et al., other works have shown related results pointing towards the understanding of how rapid laser heating changes soot and its optical properties [56, 67, 92]. Apart from changing the physical nano-structure of the soot, sublimation will also occur if high enough temperatures are reached, hence mass will be lost. In [55] and [56] it was shown by using an SMPS that size distributions showed a new mode of very small particles (~10 nm) appear when the soot had been laser heated above a certain threshold. The new mode was assigned to newly formed particles from vaporized species which were shown to have relatively low level of order in relation to the parent soot particles. In *Paper IV*, it is further explored how young mini-CAST soot responds to rapid laser heating. One purpose was to investigate the possibility of evaporating volatile species from the soot prior to LII measurements, another to study the potential annealing of young

soot and indirectly enhance the detectability of the soot with weak absorption properties.

**Figure 4.12** shows a series of measurements where the fluence curves are shown for OP1, OP6 and OP7 soot with a pre-heating laser of 532 nm and a LII excitation laser at 1064 nm. The black dots show the fluence curves of the unaltered soot directly from the mini-CAST, while the blue markers show the pre-heated soot of different pre-heating energies as specified in the figure legend.

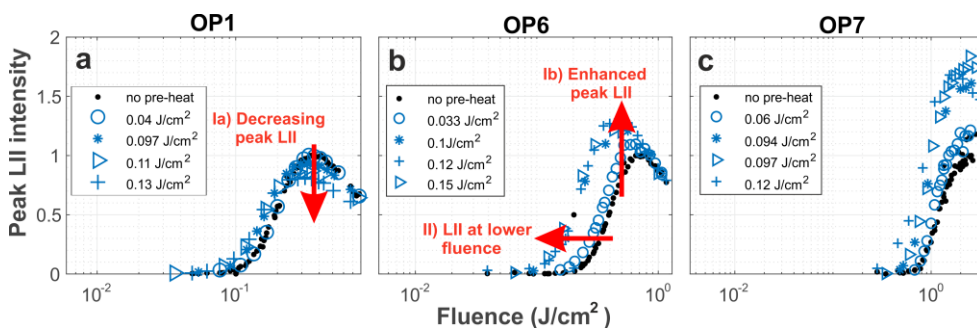


**Figure 4.12.** The fluence curves are shown for **a** OP1, **b** OP6 and **c** OP7 soot. The fluence curves of plain soot is shown as black dots, while for the pre-heated soot blue markers are used. As the soot is pre-heated, the fluence curves will change, these trends with heating energy are indicated by the red arrows.

The changed appearance of the fluence curves as a result of a pre-heating laser-pulse are represented by I) a change in peak LII intensity and II) a shift along the fluence axis. As discussed in *Paper IV*, sublimation, annealing, a subsequent change of optical properties, and evaporation of volatile species are responsible for the induced changes. The trends for the different types of soot are the same considering the shift along the fluence axis, as all types of soot appear to have enhanced absorption properties after being pre-heated. Considering the peak LII signal however, differences appear depending on the level of maturity. For the mature soot, it appears that the peak LII signal has a decreasing trend as a result of substantial sublimation from the first laser pulse. For OP6 and OP7 soot however, the first pulse leads to annealing and the resulting enhanced absorption and emissivity induce a higher LII signal.

The overall trends are shown in **Figure 4.13** where the trends of the 50 ns delayed fluence curves are also included (to eliminate potential influence of peak signal interference of the PMTs). The peak LII intensity decreases at lower pre-heating energies for the more mature soot, while for the younger soot the decreasing trend occurs at higher pre-heat energies. The competing influence of thermal annealing and hence an enhanced LII signal appears more dominant for the less mature soot.

**Figure 4.13 b** shows that pre-heating of soot leads to an increasing absorption efficiency for all types of soot based on fluence curve analysis.

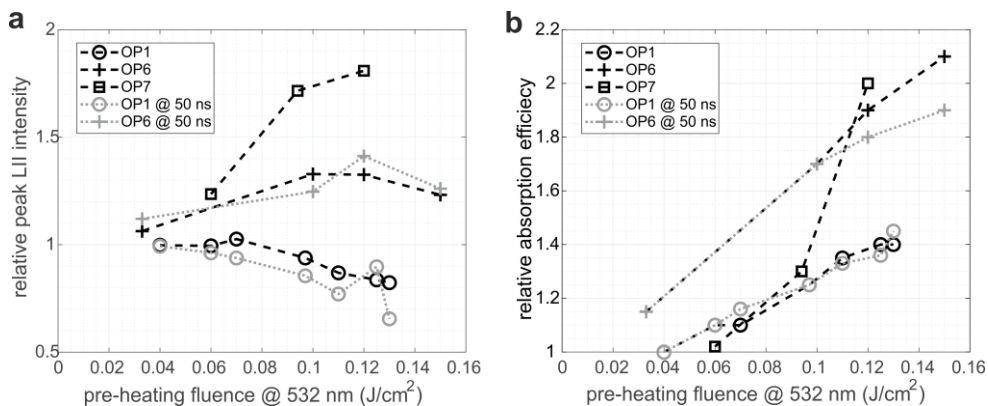


**Figure 4.13.** The trends in Figure 4.12 are here shown for all OP soot, based on the 1064 nm fluence curves with 532 nm pre-heating. In **a**, the relative peak intensity is shown as a function of pre-heating energy. In **b**, the relative absorption efficiency is shown for the same data. To be on the safe side, the trends of the delayed fluence curves are also included and show good agreement with the trends based on the peak LII.

The same analysis may be done for all combinations of heating and excitation wavelengths by considering the trends for the delayed fluence curves. In **Figure 4.14** the absorption efficiency trends are shown for OP1 by shifting the results of the 1064 nm data according to the estimated wavelength dependence ( $\zeta$ ) in **Figure 4.10**. It can be observed that the curves have their origin in the same region, but with increasing pre-heating energy, the curves split up, suggesting a change of  $\zeta$ , the more pre-heated the soot is. And the more pre-heated the soot is, the more extensively it is thermally annealed. In the current analysis a simple linear relationship is assumed, which at least provides a rough estimation and can be used to estimate the dispersion coefficient of the soot as a function of pre-heating energy. This evolution is shown as the blue graph connected to the right y-axis of **Figure 4.14**. The same analysis was performed for OP6 soot and a similar behaviour was observed providing a change of the dispersion coefficient from 1.66 to 1.41 at 0.12 J/cm<sup>2</sup> as compared to 1.17 to 1 at 0.12 J/cm<sup>2</sup> for OP1 soot as can be seen below.

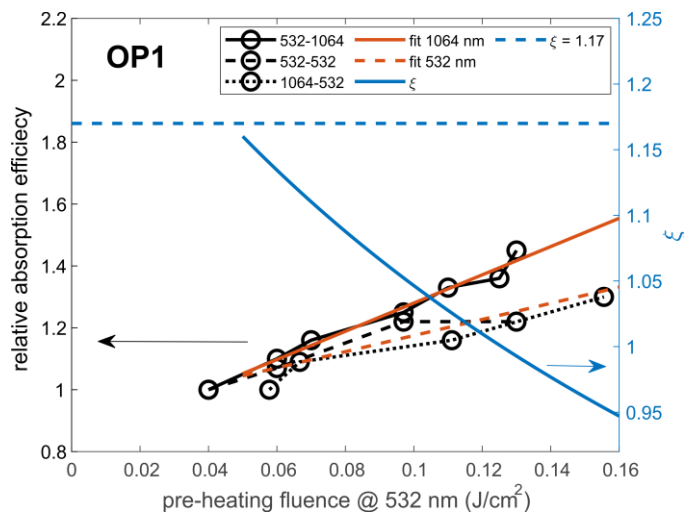


**Figure 4.14.** The relative absorption efficiency is shown for all types of soot, where the trends are based on the delayed fluence curves. As the curves split up due to the difference in wavelength, a change in  $\xi$  is expected. Hence, the change of  $\xi$  is evaluated and shown as the blue line.

As both sublimation and thermal annealing will influence the peak LII signal, it may be of interest to estimate the extent of mass loss, as the change of the dispersion coefficient has already been estimated. By utilizing the LII model, the mass loss for OP1 may be estimated with pre-heating of  $0.13 \text{ J/cm}^2$  ( $\sim 0.3 \text{ J/cm}^2$  at  $1064 \text{ nm}$ ) to about 16 %.

Another method for estimating the mass loss was presented in *Paper IV*, and that is leading edge fit for the elastic light scattering performed simultaneously with the LII measurements [96]. The leading edge fit is otherwise a common evaluation technique to obtain coating thickness from single particle soot photometer (SP2) measurements [73]. The resulting relative mass trends can be observed in **Figure 4.15**, where it appears that the estimation from using the LII model aligns well with the leading edge fit mass loss estimations, suggesting a sublimation threshold for OP1 at  $0.065$  and  $\sim 0.13 \text{ J/cm}^2$  for  $532 \text{ nm}$  and  $1064 \text{ nm}$  respectively, which aligns well with the later part of the low fluence regime of OP1. For OP6 however, the sublimation appears to occur at lower energies than for OP1 which is unexpected, nevertheless the mass loss estimation for young soot in a Santoro burner appears to agree relatively well with the OP6 results. It may however be challenging to interpret the results from OP6 as it consists of a high fraction of volatiles and as both optical and morphological properties of the soot will change upon pre-heating.

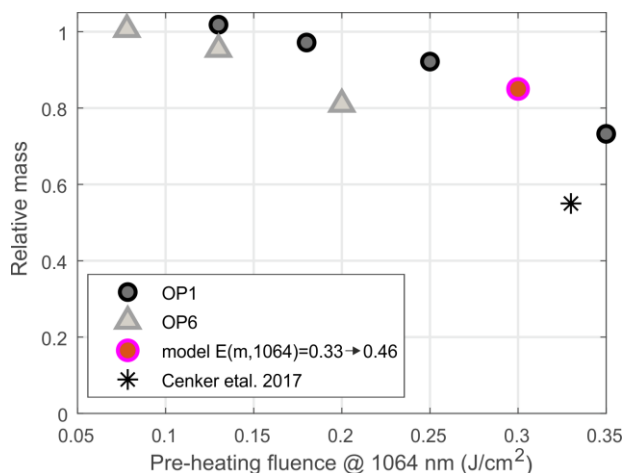


**Figure 4.15.** The estimated mass loss for OP1 and OP6 soot from analysis of the laser scattering measurements done during the LII measurements. The results are compared to estimations from LII modelling and to value provided in [92] for less mature soot in a Santoro burner.

Further the LIF contribution was considered in order to estimate its contribution to the collected LII signal when using the excitation wavelength of 532 nm and to investigate if the signal would decrease as a function of pre-heating due to evaporation of volatile species such as PAHs. As expected there was no LIF contribution to the LII signal for the OP1 soot as it has a low fraction of organics. However extensive amount of LIF signal interference to the LII signal was found for the OP6 soot as previously discussed in the earlier section about the 1-pulse experiments, where it was observed that the LIF contribution at the detection wavelength of 575 nm was up to ~50 %. When pre-heated using a laser pulse, the LIF contribution increased extensively. In **Figure 4.16**, the LII (using 1064 nm) and LII+LIF (using 532 nm) signal is shown for OP6 soot for two pre-heating pulse energies. The curves are normalized to the time resolved LII signal point at 50 ns after peak where no LIF may influence the data. It can be seen, that when low pre-heating pulse energy is used, there is no change in LIF contribution. At a high pre-heating pulse energy of 0.12 J/cm<sup>2</sup> however, and increased LIF contribution can be observed as the difference between the red curves. It is suggested to be due to evaporated species which may become fluorescing when released from the soot, or as observed in [56], due to newly formed particles of “low maturity”. It is hence of relevance to consider the experimental design of an LII setup to optimise the detection of various types of soot and avoiding laser-induced fluorescence from organics.

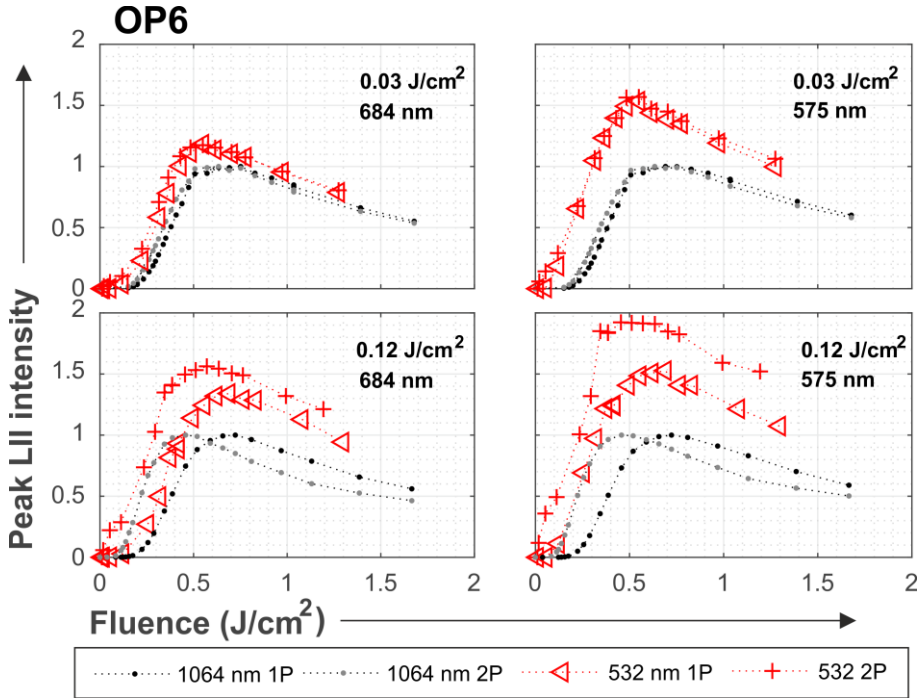


**Figure 4.16.** The LII signal using the excitation wavelength of 1064 nm is compared to the LII+LIF signal using the excitation wavelength of 532 nm. 1P denotes the 1-pulse experiments while 2-P denotes the 2-pulse experiments using a pre-heating laser pulse of the given energy. The results are shown for both detection wavelengths (575 and 684 nm). The signals are normalized to the LII signal.

### 4.2.3 Continuous wave LII (CW-LII)

In *Paper I* and *IV* it has been shown that heating processes may alter the soot in different ways; through rapid heating using laser pulse, heating in an oven, or during a thermo-optical temperature scheme. Also it has been shown in *Paper I* and *III* that the absorption properties of the different types of soot have very different absorption properties in terms of absorption efficiency ( $E(m, \lambda)$ ) and in terms of absorption wavelength dependence ( $\zeta$ ).

In recent work, a single particle soot photometer (SP2; Droplet measurement technologies, CO, USA) was used to investigate how the SP2 responds to soot of various maturity. As the soot particle passes through the beam during a period of approximately 20  $\mu\text{s}$  of an intra-cavity Nd:YAG laser at 1064 nm, it will absorb the radiation and emit an LII signal, which is detected temporally on single particle basis. As limitations of soot size and absorption properties prevented OP7 from being investigated, OP6 and OP1 soot were used. In **Figure 4.17** the experimental

and modelled CW LII signals are shown for soot aggregates of a mobility diameter of 169 nm. The difference in time and intensity of the signals may be related to the difference in absorption efficiency as the  $E(m, \lambda)$  used for the modelling are the estimated values in *Paper III*. Hence it appears that the SP2 might be able to differentiate between differently matured soot particles if the same aggregate sizes are considered (e.g. by DMA sampling). The agreement between experiments and modelling is especially good regarding the relative peak intensity and at the leading edges of the LII signals. In the modelling, constant  $E(m, \lambda)$  values have been used. However, based on the results of this thesis it is clear that the soot will be thermally annealed as it passes the laser beam in the SP2. Improved modelling should take such an effect into account, hence more work needs to be done on this matter.

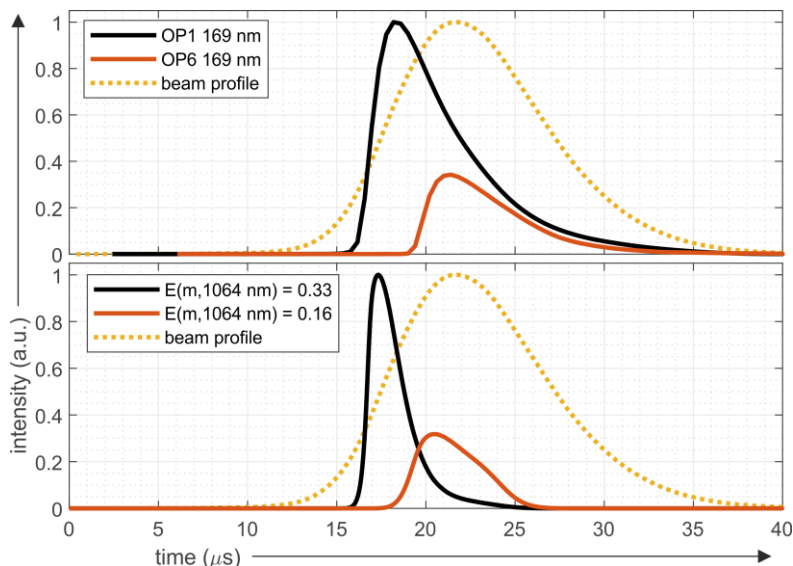


**Figure 4.17.** In the upper graph the temporal LII signal is shown for OP1 and OP6 soot of a mobility diameter of 169 nm. The beam profile is included for timing comparison. In the bottom figure, the modelled LII signal is shown for soot with the same absorption function  $E(m, 1064\text{nm})$  as estimated in *Paper III*. The results show good agreement of the signal trends.

## 5 Summary and conclusions

The work presented in this thesis has been focused on the investigation of how the optical properties of differently matured mini-CAST soot is related to its physicochemical properties. Hence, emphasis has been on the use of optical measurement techniques, where laser diagnostics has been of main importance. Another focus of the work is on the characterization of the effects of rapid laser heating of soot (of various maturities) produced by a mini-CAST soot generator, which is essential in order to understand the diagnostic potential and limitations for the laser-induced incandescence (LII) technique.

In the work presented in *Paper I*, soot from the mini-CAST soot generator showed vastly different absorption properties with an absorption wavelength dependency ( $AAE$ ,  $\zeta$ ) spanning from 1.17 to 3.5 in the wavelength range of 405-1064 nm. Heating of the soot in a thermodenuder and oven resulted in a decrease of the  $AAE$  for OP6 and OP7 soot, which was related to the decreasing OC/EC ratio of the soot. Hence, the evaporated species can partly be considered absorbing, but potential charring during heating in a thermodenuder and oven cannot be ruled out. The  $AAE$  did however not drop to 1 after heating and neither did the OC content drop to 0, hence it was discussed that the strong wavelength dependence was related to remaining OC and EC. During the heating scheme of the thermo-optical analysis enhanced absorption was observed when the young soot was present in an inert atmosphere, suggesting altering of the soot absorption properties. Analysis of the MAC-relation between the OC and EC fractions revealed that the soot of higher  $AAE$  is not composed of a mature refractory core with a BrC-like coating, but can rather be considered as refractory soot of low maturity – namely *young soot*. Comparisons were made with previous measurements in a pre-mixed laboratory McKenna flame, which showed the evolution of soot maturation and where  $AAEs$  agreed well with the various types of mini-CAST soot. Hence, the soot investigated in the work of this thesis can be considered to originate from different regimes in the brown-black continuum.

The feasibility of using a 3- $\lambda$  integrating nephelometer to obtain morphological properties of soot fractal aggregates was investigated, and presented in *Paper II*. To obtain morphological properties of the elastic light scattering (at three wavelengths and integrated in forward and backward direction) involves solving the inverse scattering problem. By utilizing RDG-theory for fractal aggregates, morphological



parameters such as  $R_g$  and  $D_f$  could be obtained when assuming a  $k_0$  and if  $R_g < 185$  nm where the majority of the scattering was not yet in the power-law regime. The developed method was tested for mini-CAST soot and compared with estimations of  $R_g$  and  $D_f$  from TEM image analysis. It was showed that the estimated  $R_g$  was somewhat over-estimated when solving the inverse method, but sources of error were identified. Discussed sources of error were, polydispersity, accuracy of the RDG-theory and sampling, which were all shown to bias the results towards an estimated larger larger  $R_g$ . The  $F(m,\lambda)$ -ratio was also estimated based on the morphology and on the SAE results and it was shown that it increased with decreasing maturity which agrees well with trends observed in the literature. This work hence shows that the method presented can be useful in obtaining information on morphology of freshly emitted soot and can be used as an *in-situ* alternative to microscopy techniques.

Further, LII was used in the work presented in *Paper III* and *IV* to study the optical properties of various soot types, and to study the induced changes in the properties of young as well as mature soot by rapid laser heating. By fluence curve analysis of differently matured soot, obtained at two laser wavelengths (532 and 1064 nm), the absorption wavelength dependence  $\zeta$  was investigated and compared to AAE estimations in *Paper I*. Good agreement was observed for the mature soot, while for young soot  $\zeta$  appeared somewhat lower in comparison with multi- $\lambda$  extinction measurements. Discussions regarding different reasons for the discrepancies were 1) the influence of rapid laser heating potentially altering the soot by e.g. annealing, and 2) the influence by the difference in used wavelengths. The absorption efficiency was investigated for OP1 by evaluation of  $E(m,\lambda)$  in the low fluence regime. The evolution of the LII temperature which increases linearly prior to extensive sublimation is considered in a region where the volumetric heat capacity can be considered constant. The LII model was used to further investigate  $E(m,\lambda)$  for OP6 and OP7 by fluence curve analysis and the potential influence of volatiles was considered to have a minor influence on the estimations. The absorption properties of differently matured soot was hence shown to span over the brown-black continuum as mature OP1 soot had an  $E(m,\lambda) = 0.33$ , as compared to OP7 soot with  $E(m,\lambda) = 0.05$ . This large variation has to be considered when performing LII in sooty environments. Further, it has to be investigated at what time frame soot properties may be changed when rapidly heated with a short laser pulse.

In *Paper IV*, work was presented where 2-pulse LII experiments were conducted to investigate how rapid laser heating influences young as well as mature soot, mainly in relation to LII measurements. It was observed that the pre-heating pulse enhanced the absorption efficiency for young as well as mature soot as a result of thermal annealing, with a stronger effect for the young soot. Another effect of the pre-heating pulse for young soot was the observation of an increased laser-induced fluorescence, probably originating from evaporated species/soot fragments/re-

condensed particles when using LII at 532 nm. This fluorescence was negligible for the mature soot. As two excitation wavelengths were used both for pre-heating and for the LII measurements estimations of  $\zeta$  as a function of pre-heating could be done. It was shown that pre-heating did indeed induce a decrease of  $\zeta$  which can be related to thermal annealing. Laser pre-heating would also induce mass loss due to potential evaporation of volatile species, but also sublimation which was significant especially for the mature soot. Mass loss estimations of mature soot, based on the simultaneous measurement of scattering during LII agreed well with mass loss estimations based on LII modelling. Mass loss of young soot however is complex and scattering measurements could not provide information on the matter. The work in *Paper IV* hence shows, that rapid laser heating can indeed have large influence on soot of different maturity and hence, the principle of two-pulse experiment may be useful in terms of enhancing the detectability of poorly absorbing soot when performing LII in sooty environments.



## 6 Outlook

Brown carbon has been shown to be an important pollutant in addition to BC, since it may be a significant contributor to a positive radiative forcing [12]. As the BrC-BC spectrum can range over large span of optical and physicochemical properties, caution has to be taken when performing measurements on e.g. BrC-type of soot or on combustion aerosols of unknown character, as measurement techniques may originally have been developed for mature soot. As has been shown, mini-CAST soot can range from BrC-type of soot (young soot), to (mature) BC-like soot. Since the development of the mini-CAST used in this work, another mini-CAST have been developed with the capability of generating soot more resembling the range of real life soot [97]. Nevertheless, mini-CAST soot generators such as the one used in this work, provides soot with a wide range of optical and physicochemical properties useful for characterization and testing of diagnostic tools to investigate their response to differently matured soot.

It was shown that rapid laser heating of soot, will when reaching high temperatures, change the optical properties of the soot and hence become intrusive. It is hence of great importance to acknowledge this, as further diagnostics on the same probe volume may give different results than it would prior to laser heating as pointed out by [95]. For CW-LII measurements, e.g. with SP2, the influence of laser heating occurs during measurements as the time range of measurements is on the  $\mu\text{s}$  scale. The influence of thermal annealing should occur for soot of all levels of maturity, but potentially at a lower temperature for the young soot. Hence, despite the potential influence on the soot, the SP2 appears very interesting in terms of soot diagnostics as single particle LII can be observed. Due to the difference in absorption efficiency of differently matured soot, SP2 appears to be sensitive to the maturity of soot as shown in the results section, which would be valuable when using the instrument for real-life soot emissions. The influence of coating may however complicate the matter of evaluating the maturity of individual soot cores from SP2 measurements, and further work is needed on this matter.

The intrusiveness of rapid laser heating as done during LII measurements could possibly also be considered useful, as it enhances the detectability of otherwise poorly absorbing soot particles. Potentially a double-pulse technique could be further developed to enhance the detectability of brown carbon. Another option to detect brown carbon is as discussed in this thesis laser-induced fluorescence. A

question may be, what actually does fluoresce when performing LIF on young soot. PAHs are known to fluoresce strongly and are usually used as a proxy for the region of early soot formation, but does condensed matter such as incipient and young soot also fluoresce themselves and contribute significantly to an overall LIF signal? Perhaps combinations of 2-pulse LII and LIF can contribute to the understanding of the early soot formation processes?

The nephelometer is a relatively common tool in the field of atmospheric monitoring and research, and appears to be able to provide information on morphological parameters of freshly emitted soot. It may hence be a useful tool to obtain this type of information in real time as it operates *in-situ*, as compared to TEM analysis which is more demanding. Further work on size selected soot should however be done, to investigate the limitations of the method. It would also be highly interesting to look into data from real combustion sources where the soot has not yet been coated and hence possibly not collapsed yet, to investigate the usefulness of the technique in the field. Also, more advanced nephelometers are available on the market for which more angle-resolved scattering information can be obtained.

However, before implementing knowledge from the presented work and proceed with atmospheric observations, a first next step should be to increase the level of soot aerosol complexity, and learn about the influence of coating and atmospheric ageing in controlled experiments. Then, insights on the possibilities and limitations of soot aerosol diagnostics such as SP2 e.g. can be obtained. Then applications useful in the field can be identified and be used in atmospheric observations and research.

# Bibliography

1. T.C. Bond, et al., Bounding the role of black carbon in the climate system: A scientific assessment. *Journal of Geophysical Research: Atmospheres*. 118 (11) (2013) 5380-5552.
2. IPCC, *Climate Change 2013: The Physical Science Basis. Contribution of Working Group I to the Fifth Assessment Report of the Intergovernmental Panel on Climate Change*. 2013, Cambridge, United Kingdom and New York, NY, USA: Cambridge University Press. 1535.
3. K.-H. Kim, et al., A review of airborne polycyclic aromatic hydrocarbons (PAHs) and their human health effects. *Environment International*. 60 (2013) 71-80.
4. M. Shiraiwa, et al., Hazardous components and health effects of atmospheric aerosol particles: reactive oxygen species, soot, polycyclic aromatic compounds and allergenic proteins. *Free Radical Research*. 46 (8) (2012) 927-939.
5. WHO *7 million premature deaths annually linked to air pollution*. 2014.
6. W.C. Hinds, *Aerosol technology: properties, behavior, and measurement of airborne particles*. 1999: John Wiley & Sons.
7. H.D. Matthews, et al., Climate response to zeroed emissions of greenhouse gases and aerosols. *Nature Climate Change*. 2 (5) (2012) 338-341.
8. D. Shindell, et al., Climate and air-quality benefits of a realistic phase-out of fossil fuels. *Nature*. 573 (7774) (2019) 408-411.
9. H.A. Michelsen, et al., A Review of Terminology Used to Describe Soot Formation and Evolution under Combustion and Pyrolytic Conditions. *ACS Nano*. 14 (10) (2020) 12470-12490.
10. J.C. Corbin, et al., Infrared-absorbing carbonaceous tar can dominate light absorption by marine-engine exhaust. *npj Climate and Atmospheric Science*. 2 (1) (2019) 12.
11. A. Laskin, et al., Chemistry of Atmospheric Brown Carbon. *Chemical Reviews*. 115 (10) (2015) 4335-4382.
12. R. Saleh, From measurements to models: toward accurate representation of brown carbon in climate calculations. *Current Pollution Reports*. 6 (2) (2020) 90-104.
13. R. Saleh, et al., The Brown–Black Continuum of Light-Absorbing Combustion Aerosols. *Environmental Science & Technology Letters*. 5 (8) (2018) 508-513.

14. A. Ångström, On the Atmospheric Transmission of Sun Radiation and on Dust in the Air. *Geografiska Annaler*. 11 (1929) 156-166.
15. H. Wang, Formation of nascent soot and other condensed-phase materials in flames. *P Combust Inst.* 33 (1) (2011) 41-67.
16. M. Frenklach, et al., On the mechanism of soot nucleation. *Physical Chemistry Chemical Physics*. 22 (9) (2020) 5314-5331.
17. M. Frenklach, Reaction mechanism of soot formation in flames. *Physical chemistry chemical Physics*. 4 (11) (2002) 2028-2037.
18. K.O. Johansson, et al., Resonance-stabilized hydrocarbon-radical chain reactions may explain soot inception and growth. *Science*. 361 (6406) (2018) 997-1000.
19. A. Faccinetto, et al., Evidence on the formation of dimers of polycyclic aromatic hydrocarbons in a laminar diffusion flame. *Communications Chemistry*. 3 (1) (2020) 112.
20. X. Mercier, et al., Dimers of polycyclic aromatic hydrocarbons: the missing pieces in the soot formation process. *Physical Chemistry Chemical Physics*. 21 (16) (2019) 8282-8294.
21. A.S. Semikhin, et al., On the mechanism of soot nucleation. II. E-bridge formation at the PAH bay. *Physical Chemistry Chemical Physics*. 22 (30) (2020) 17196-17204.
22. H.A. Michelsen, et al., A Review of Terminology Used to Describe Soot Formation and Evolution under Combustion and Pyrolytic Conditions. *ACS Nano*. (2020).
23. H.A. Michelsen, Probing soot formation, chemical and physical evolution, and oxidation: A review of in situ diagnostic techniques and needs. *P Combust Inst.* 36 (1) (2017) 717-735.
24. M.O. Andreae, et al., Black carbon or brown carbon? The nature of light-absorbing carbonaceous aerosols. *Atmos. Chem. Phys.* 6 (10) (2006) 3131-3148.
25. L. Durdina, et al., Response of Real-Time Black Carbon Mass Instruments to Mini-CAST Soot. *Aerosol Science and Technology*. 50 (2016) 906-918.
26. A. Mamakos, et al., Characterization of combustion aerosol produced by a Mini-CAST and treated in a catalytic stripper. *Aerosol Science and Technology*. 47 (8) (2013) 927-936.
27. R.H. Moore, et al., Mapping the operation of the miniature combustion aerosol standard (Mini-CAST) soot generator. *Aerosol Science and Technology*. 48 (5) (2014) 467-479.
28. M.M. Maricq, Examining the relationship between black carbon and soot in flames and engine exhaust. *Aerosol Science and Technology*. 48 (6) (2014) 620-629.
29. M. Saffaripour, et al., Raman spectroscopy and TEM characterization of solid particulate matter emitted from soot generators and aircraft turbine engines. *Aerosol Science and Technology*. 51 (4) (2017) 518-531.

30. Jing. *Mini-CAST soot generator*. 2009 [cited 2019 October]; Available from: <http://www.sootgenerator.com/>.
31. Ö.L. Gülder, et al., Influence of nitrogen dilution and flame temperature on soot formation in diffusion flames. *Combustion and Flame*. 92 (1) (1993) 115-124.
32. Q. Wang, et al., Experimental characterization of the different nitrogen dilution effects on soot formation in ethylene diffusion flames. *P Combust Inst*. 36 (2) (2017) 3227-3235.
33. C.F. Bohren, et al., *Absorption and Scattering of Light by Small Particles*. 2008: Wiley.
34. C. Sorensen, Light scattering by fractal aggregates: a review. *Aerosol Science & Technology*. 35 (2) (2001) 648-687.
35. B.E. Saleh, et al., *Fundamentals of photonics*. 2007: John Wiley & Sons.
36. K. Wan, et al., Quantum confinement and size resolved modeling of electronic and optical properties of small soot particles. *P Combust Inst*. (2020).
37. F. Liu, et al., Review of recent literature on the light absorption properties of black carbon: Refractive index, mass absorption cross section, and absorption function. *Aerosol Science and Technology*. 54 (1) (2020) 33-51.
38. R. Saleh, et al., Brownness of organics in aerosols from biomass burning linked to their black carbon content. *Nature Geoscience*. 7 (9) (2014) 647-650.
39. C. Liu, et al., Flame-formed carbon nanoparticles exhibit quantum dot behaviors. *Proceedings of the National Academy of Sciences*. 116 (26) (2019) 12692-12697.
40. A. Bescond, et al., Soot optical properties determined by analyzing extinction spectra in the visible near-UV: Toward an optical speciation according to constituents and structure. *Journal of Aerosol Science*. 101 (2016) 118-132.
41. C.M. Sorensen, et al., Light scattering and absorption by fractal aggregates including soot. *Journal of Quantitative Spectroscopy and Radiative Transfer*. 217 (2018) 459-473.
42. T.C. Bond, et al., Light absorption by carbonaceous particles: An investigative review. *Aerosol science and technology*. 40 (1) (2006) 27-67.
43. J. Simonsson, et al., Wavelength dependence of extinction in sooting flat premixed flames in the visible and near-infrared regimes. *Applied Physics B*. 119 (4) (2015) 657-667.
44. C. Russo, et al., Optical band gap analysis of soot and organic carbon in premixed ethylene flames: Comparison of in-situ and ex-situ absorption measurements. *Carbon*. 158 (2020) 89-96.
45. A. Menon, et al., Optical band gap of cross-linked, curved, and radical polyaromatic hydrocarbons. *Physical Chemistry Chemical Physics*. 21 (29) (2019) 16240-16251.



46. Ü.Ö. Köylü, et al., Fractal and projected structure properties of soot aggregates. *Combustion and Flame*. 100 (4) (1995) 621-633.
47. M. Kahnert, et al., Modelling optical properties of atmospheric black carbon aerosols. *Journal of Quantitative Spectroscopy and Radiative Transfer*. 244 (2020) 106849.
48. H.A. Michelsen, et al., Laser-induced incandescence: Particulate diagnostics for combustion, atmospheric, and industrial applications. *Progress in Energy and Combustion Science*. 51 (2015) 2-48.
49. X. López-Yglesias, et al., Soot maturity and absorption cross sections. *Journal of Aerosol Science*. 75 (2014) 43-64.
50. C. Schulz, et al., Laser-induced incandescence: recent trends and current questions. *Applied Physics B*. 83 (3) (2006) 333.
51. H.A. Michelsen, Understanding and predicting the temporal response of laser-induced incandescence from carbonaceous particles. *The Journal of chemical physics*. 118 (15) (2003) 7012-7045.
52. H.A. Michelsen, Effects of maturity and temperature on soot density and specific heat. *P Combust Inst*. (2020).
53. S. De Iuliis, et al., Peak soot temperature in laser-induced incandescence measurements. *Applied Physics B*. 83 (3) (2006) 397.
54. N.-E. Olofsson, et al., Evolution of properties for aging soot in premixed flat flames studied by laser-induced incandescence and elastic light scattering. *Applied Physics B*. 119 (4) (2015) 669-683.
55. H.A. Michelsen, et al., Particle formation from pulsed laser irradiation of soot aggregates studied with a scanning mobility particle sizer, a transmission electron microscope, and a scanning transmission x-ray microscope. *Appl. Opt*. 46 (6) (2007) 959-977.
56. F. Migliorini, et al., Nanosecond laser irradiation of soot particles: Insights on structure and optical properties. *Experimental Thermal and Fluid Science*. 114 (2020) 110064.
57. J.P. Abrahamson, et al., Pulsed laser annealing of carbon black. *Carbon*. 124 (2017) 380-390.
58. H. Bladh, et al., On the dependence of the laser-induced incandescence (LII) signal on soot volume fraction for variations in particle size. *Applied Physics B*. 90 (1) (2008) 109-125.
59. G.J. Smallwood, et al., Clouds Over Soot Evaporation: Errors in Modeling Laser-Induced Incandescence of Soot. *Journal of Heat Transfer*. 123 (4) (2000) 814-818.
60. H.R. Leider, et al., Thermodynamic properties of carbon up to the critical point. *Carbon*. 11 (5) (1973) 555-563.
61. F. Liu, et al., Influence of polydisperse distributions of both primary particle and aggregate size on soot temperature in low-fluence LII. *Applied Physics B*. 83 (3) (2006) 383.

62. J. Johnsson, et al., Influence of soot aggregate structure on particle sizing using laser-induced incandescence: importance of bridging between primary particles. *Applied Physics B*. 112 (3) (2013) 321-332.
63. R.P. Bambha, et al., Effects of aggregate morphology and size on laser-induced incandescence and scattering from black carbon (mature soot). *Journal of Aerosol Science*. 88 (2015) 159-181.
64. R.L. Vander Wal, Laser-induced incandescence: excitation and detection conditions, material transformations and calibration. *Applied Physics B*. 96 (4) (2009) 601-611.
65. R.L. Vander Wal, et al., Pulsed laser heating of soot: morphological changes. *Carbon*. 37 (2) (1999) 231-239.
66. R.L. Vander Wal, et al., Optical and microscopy investigations of soot structure alterations by laser-induced incandescence. *Applied Physics B*. 67 (1) (1998) 115-123.
67. B. Apicella, et al., Laser-induced structural modifications of differently aged soot investigated by HRTEM. *Combustion and Flame*. 204 (2019) 13-22.
68. H. Bladh, et al., Characteristics of laser-induced incandescence from soot in studies of a time-dependent heat- and mass-transfer model. *Applied Physics B*. 78 (2) (2004) 241-248.
69. R. Mansmann, et al., Performance of photomultipliers in the context of laser-induced incandescence. *Appl. Opt.* 56 (28) (2017) 7849-7860.
70. R.P. Bambha, et al., Effects of volatile coatings and coating removal mechanisms on the morphology of graphitic soot. *Carbon*. 61 (2013) 80-96.
71. Ü.Ö. Köylü, et al., Optical properties of overfire soot in buoyant turbulent diffusion flames at long residence times. (1994).
72. E.P. Ltd, *Aurora 3000 Multi Wavelength Integrating Nephelometer (with backscatter)*. 2013.
73. R. Gao, et al., A novel method for estimating light-scattering properties of soot aerosols using a modified single-particle soot photometer. *Aerosol Science and Technology*. 41 (2) (2007) 125-135.
74. L. Drinovec, et al., The "dual-spot" Aethalometer: an improved measurement of aerosol black carbon with real-time loading compensation. *Atmos. Meas. Tech.* 8 (5) (2015) 1965-1979.
75. C. Sorensen, The mobility of fractal aggregates: a review. *Aerosol Science and Technology*. 45 (7) (2011) 765-779.
76. T.B. Onasch, et al., Soot particle aerosol mass spectrometer: development, validation, and initial application. *Aerosol Science and Technology*. 46 (7) (2012) 804-817.
77. V.B. Malmborg, et al., Relating aerosol mass spectra to composition and nanostructure of soot particles. *Carbon*. 142 (2019) 535-546.
78. F. Cavalli, et al., Toward a standardised thermal-optical protocol for measuring atmospheric organic and elemental carbon: the EUSAAR protocol. *Atmospheric Measurement Techniques*. 3 (1) (2010) 79-89.

79. T. Haller, et al., Structural changes of CAST soot during a thermal–optical measurement protocol. *Atmospheric Measurement Techniques*. 12 (7) (2019) 3503-3519.
80. T. Haller, et al., Investigation of structural changes of atmospheric aerosol samples during two thermal–optical measurement procedures (EUSAAR2, NIOSH870). *Atmospheric Measurement Techniques*. 14 (5) (2021) 3721-3735.
81. H. Oltmann, et al., Wide-angle light scattering (WALS) for soot aggregate characterization. *Combustion and Flame*. 157 (3) (2010) 516-522.
82. M. Altenhoff, et al., Soot aggregate sizing in an extended premixed flame by high-resolution two-dimensional multi-angle light scattering (2D-MALS). *Applied Physics B*. 125 (9) (2019) 176.
83. P. Kheirkhah, et al., Development and validation of a multi-angle light scattering method for fast engine soot mass and size measurements. *Aerosol Science and Technology*. 54 (9) (2020) 1083-1101.
84. S. Talebi-Moghaddam, et al., Inferring soot morphology through multi-angle light scattering using an artificial neural network. *Journal of Quantitative Spectroscopy and Radiative Transfer*. 251 (2020) 106957.
85. J. Kim, et al., Assessing Optical Properties and Refractive Index of Combustion Aerosol Particles Through Combined Experimental and Modeling Studies. *Aerosol Science and Technology*. 49 (5) (2015) 340-350.
86. Ü. Köylü, et al., Fractal morphology analysis of combustion-generated aggregates using angular light scattering and electron microscope images. *Langmuir*. 11 (12) (1995) 4848-4854.
87. S. Bejaoui, et al., Laser induced fluorescence spectroscopy of aromatic species produced in atmospheric sooting flames using UV and visible excitation wavelengths. *Combustion and Flame*. 161 (10) (2014) 2479-2491.
88. G. Cléon, et al., Laser induced incandescence determination of the ratio of the soot absorption functions at 532 nm and 1064 nm in the nucleation zone of a low pressure premixed sooting flame. *Applied Physics B: Lasers and Optics*. 104 (2) (2011) 297-305.
89. E. Therssen, et al., Determination of the ratio of soot refractive index function  $E(m)$  at the two wavelengths 532 and 1064 nm by laser induced incandescence. *Applied Physics B*. 89 (2) (2007) 417-427.
90. R.P. Bambha, et al., Effects of volatile coatings on the laser-induced incandescence of soot. *Applied Physics B*. 112 (3) (2013) 343-358.
91. F. Goulay, et al., A data set for validation of models of laser-induced incandescence from soot: temporal profiles of LII signal and particle temperature. *Applied Physics B*. 112 (3) (2013) 287-306.
92. E. Cenker, et al., Quantitative effects of rapid heating on soot-particle sizing through analysis of two-pulse LII. *Applied Physics B*. 123 (3) (2017) 74.
93. M. Saffaripour, et al., Influence of rapid laser heating on the optical properties of in-flame soot. *Applied Physics B*. 119 (4) (2015) 621-642.

94. K. Thomson, et al., Optical properties of pulsed laser heated soot. *Applied Physics B*. 104 (2) (2011) 307-319.
95. E. Cenker, et al., Investigations of the long-term effects of LII on soot and bath gas. *Aerosol Science and Technology*. 51 (12) (2017) 1354-1367.
96. P.O. Witze, et al., Time-resolved laser-induced incandescence and laser elastic-scattering measurements in a propane diffusion flame. *Appl. Opt.* 40 (15) (2001) 2443-2452.
97. M.N. Ess, et al., Optical and morphological properties of soot particles generated by the miniCAST 5201 BC generator. *Aerosol Science and Technology*. (2021) 1-25.



# Acknowledgements

First and foremost I want to thank my supervisor Per-Erik Bengtsson. Thank you for everything! For the support, the laughs, the kindness, the understanding, the inspiration and, the opportunity for me to take this journey. Thank you Per-Erik.

I would also like to thank Joakim Pagels, my co-supervisor for all the support and good discussions on e.g. BC, BrC, VOC, OC, EC, PC, OA, eBC, rBC and MAC. Also I would like to thank Henrik Bladh my co-supervisor during my first year at the division. Thank you for the LII model, oh how would we manage without it!

I would like to thank the most amazing colleagues, it has been such a pleasure to be in the soot group with you. Thank you Thi Kim Cuong Le, for the kind and amazing researcher that you are. Manu Mannazhi, thanks for sharing time and lab during busy times and for always being so nice! Saga Bergqvist, thanks for good times and for inspiring me to do crafts and grow new things! I would also like to thank the old soot group members Nils-Erik Olofsson for your nice work on sublimation temperatures and Johan Simonsson for good times in Alcatraz and many in the lab.

Further I want to thank Vilhelm Malmberg for great times in the lab, and for many interesting discussions. Thank you Axel Eriksson for being kind and inclusive when I was a newly hatched PhD student. And thank you Erik Ahlberg, Lovisa Nilsson and Erik Swietlicki for new exciting adventures in the world of single particle detection. Thank you Anders Karlsson and Adrian Roth for the great collaboration and endless number of meetings, we made it!

Thank you my dear office mate, Yupan Bao. It has been such a pleasure sharing the office with you! And thank you Stephanie Polster and Anna-Lena Sahlberg for good office times back in the days.

Thank you Marcus Aldén, Minna Ramkull, Cecilia Bille, Igor Buzuk, Rutger Larsson, Fredrik Ossler, Robert Collin and Sven-Inge Möller for having made and some still making this division such an amazing and safe work-place, and for all the support in many different ways.

I want to thank Dina Hot, for being a good friend, for the good times and for all the support throughout the times at the division!

I would further like to thank Panagiota Stamatoglou, Jianfeng Zhou, Per Samuelsson, David Sanned, Henrik Feuk, Mikkel Brydegaard, Elin Malmqvist, Samuel Jönsson, Maria Ruchkina, Saeed Derafshzan, Haisol Kim, Xin Liu, Shen Li, Arman Subash, Christian Brackmann, Eduoard Berrocal, Marco Lubrano Lavadera, Christoffer Pichler, Mattias Richter and Secret Santa for many different reasons such as great teaching experience, helping out, good collaborations, fun times, hanging out and nice lunches.

Finally I would like to thank my family, but especially my mum and dad for the endless support. I could never ever have done this without you. <3

And thank you Klaes, for all of the support and for being by my side throughout this journey. <3

And my children, thank you for everything! <3







Faculty of Engineering  
Department of Physics  
Division of Combustion Physics

Lund Reports on Combustion Physics, LRCP-236 (2021)  
ISRN LUTFD2/TFCP-236-SE  
ISBN 978-91-7895-971-6 (print)  
ISSN 1102-8718

